eprints@whiterose.ac.uk
https://eprints.whiterose.ac.uk/

Observation of many-body scarring in a Bose-Hubbard quantum simulator

Guo-Xian Su,[1, 2, 3] Hui Sun,[1, 2, 3] Ana Hudomal,[4, 5] Jean-Yves Desaules,[4] Zhao-Yu Zhou,[1, 2, 3] Bing Yang,[6] Jad C. Halimeh,[7] Zhen-Sheng Yuan,[1, 2, 3, *] Zlatko Papić,[4, †] and Jian-Wei Pan[1, 2, 3, ‡]

[1]*Hefei National Laboratory for Physical Sciences at Microscale and Department of Modern Physics,*
University of Science and Technology of China, Hefei, Anhui 230026, China
[2]*Physikalisches Institut, Ruprecht-Karls-Universität Heidelberg,*
Im Neuenheimer Feld 226, 69120 Heidelberg, Germany
[3]*CAS Center for Excellence and Synergetic Innovation Center in Quantum Information and Quantum Physics,*
University of Science and Technology of China, Hefei, Anhui 230026, China
[4]*School of Physics and Astronomy, University of Leeds, Leeds LS2 9JT, UK*
[5]*Institute of Physics Belgrade, University of Belgrade, 11080 Belgrade, Serbia*
[6]*Department of Physics, Southern University of Science and Technology, Shenzhen 518055, China*
[7]*INO-CNR BEC Center and Department of Physics,*
University of Trento, Via Sommarive 14, I-38123 Trento, Italy
(Dated: March 22, 2023)

The ongoing quest for understanding nonequilibrium dynamics of complex quantum systems underpins the foundation of statistical physics as well as the development of quantum technology. Quantum many-body scarring has recently opened a window into novel mechanisms for delaying the onset of thermalization by preparing the system in special initial states, such as the $\mathbb{Z}_2$ state in a Rydberg atom system. Here we realize many-body scarring in a Bose–Hubbard quantum simulator from previously unknown initial conditions such as the unit-filling state. We develop a quantum-interference protocol for measuring the entanglement entropy and demonstrate that scarring traps the many-body system in a low-entropy subspace. Our work makes the resource of scarring accessible to a broad class of ultracold-atom experiments, and it allows to explore its relation to constrained dynamics in lattice gauge theories, Hilbert space fragmentation, and disorder-free localization.

I. INTRODUCTION

Coherent manipulation of quantum many-body systems far from equilibrium is key to unlocking outstanding problems in quantum sciences including strongly-coupled quantum field theories, exotic phases of matter, and development of enhanced metrology and computation schemes. These efforts, however, are frequently plagued by the presence of interactions in such systems, which lead to fast thermalization and information scrambling – the behavior known as quantum ergodicity [1–3]. A twist came with recent advances in synthetic quantum matter, which enabled detailed experimental study of thermalization dynamics in isolated quantum many-body systems, leading to the observation of ergodicity-violating phenomena in integrable [4] and many-body localized systems [5, 6].

More recently, quantum many-body scarring has emerged as another remarkable ergodicity-breaking phenomenon, where preparing the system in special initial states effectively traps it in a "cold" subspace that does not mix with the thermalizing bulk of the spectrum [7, 8]. Such behavior hinders the scrambling of information encoded in the initial state and suppresses the spreading of quantum entanglement, allowing a many-body system to display persistent quantum revivals. Many-body scarring was first observed in the Rydberg atom experimental platform [9, 10] and subsequent observations of weak ergodicity breaking phenomena have attracted much attention [11–13]. On the other hand, theoretical works have unearthed universal scarring mechanisms [14–17], pointing to the ubiquity of scarring phenomena in periodically-driven systems [18–20] and in the presence of disorder [21, 22]. Given that many-body scarring in Rydberg atom systems has previously been reported in a single initial state – the $\mathbb{Z}_2$-ordered state, many questions remain about the overall fragility of this phenomenon and its sensitivity to the initial condition. It is thus vital to extend the realm of scarring to a greater variety of experimental platforms and more accessible initial conditions, which would empower fundamental understanding of nonergodic dynamics in various research areas ranging from lattice gauge theories to constrained glassy systems.

In this work, we observe many-body scarring in a large-scale Bose–Hubbard quantum simulator, where we employ a tilted optical lattice to emulate the PXP model, a canonical model of many-body scarring [23–26]. We demonstrate that many-body scarring can result from a larger set of initial states, including the unit-filling state at finite detuning, hitherto believed to undergo fast thermalization [9]. Furthermore, we demonstrate that periodic driving can be used to enhance scarring behavior. Taking advantage of spin-dependent optical superlattices, we measure the system's entanglement entropy by interfering identical copies in the double wells. We show the average entropy of single-site subsystems to be a good approximation of half-chain bipartite entropy, re-

vealing a key property of scarring: the "trapping" of the quantum system in a low-entropy subspace, which prevents its relaxation into the exponentially large Hilbert space.

The remainder of this paper is organized as follows. In Sec. II we introduce our experimental setup and show how it can realize the PXP model. In Sec. III we benchmark our quantum simulation by observing many-body scarring from the previously known $\mathbb{Z}_2$ initial state. We also demonstrate the enhancement of scarring under periodic driving. In Sec. IV we present our measurements of entanglement entropy, providing deeper insight into the slow thermalization dynamics associated with scarred initial states. Finally, in Sec. V we observe a new scarring regime at moderate detuning for the unit-filling initial state. Our conclusions are presented in Sec. VI, while Appendixes contain derivation of the PXP mapping, further details on state preparation and measurement techniques, and numerical study of other scarred initial conditions.

II. MAPPING THE PXP MODEL ONTO THE BOSE–HUBBARD MODEL

The PXP model [27, 28] describes a kinetically constrained chain of spin-1/2 degrees of freedom. Each spin can exist in two possible states, $|\circ\rangle$, $|\bullet\rangle$ corresponding to the ground state and excited state, respectively. An array of N such spins is governed by the Hamiltonian

$$\hat{H}_{\mathrm{PXP}} = \Omega \sum_{j=1}^{N} \hat{P}_{j-1} \hat{X}_j \hat{P}_{j+1}, \tag{1}$$

where $\hat{X} = |\circ\rangle\langle\bullet| + |\bullet\rangle\langle\circ|$ is the Pauli x-matrix, describing local spin precession with frequency Ω. The projectors onto the ground state, $\hat{P} = |\circ\rangle\langle\circ|$, constrain the dynamics by allowing a spin to flip only if both of its neighbors are in the ground state.

A remarkable property of the PXP model is that it is quantum chaotic, yet it exhibits persistent quantum revivals from a highly out-of-equilibrium $|\mathbb{Z}_2\rangle \equiv |\bullet\circ\bullet\circ\dots\rangle$ initial state [23, 29–31]. The presence of revivals from a special initial state in an overall chaotic system was understood to be a many-body analog of the phenomena associated with a single particle inside a stadium billiard, where nonergodicity arises as a "scar" imprinted by a particle's classical periodic orbit [16, 32, 33]. In many-body scarred systems, eigenstates were shown to form tower structures [23]. These towers are revealed by the anomalously high overlap of eigenstates with special initial states, and their equal energy spacing is responsible for quantum revivals. While previous experiments on Rydberg atoms [9, 10] have primarily focused on the $|\mathbb{Z}_2\rangle$ initial state, we will demonstrate that the PXP model can effectively emerge in the Bose-Hubbard model, allowing us to identify scarred revivals from a larger set of initial conditions, including the polarized state $|0\rangle \equiv |\circ\circ\circ\dots\rangle$.
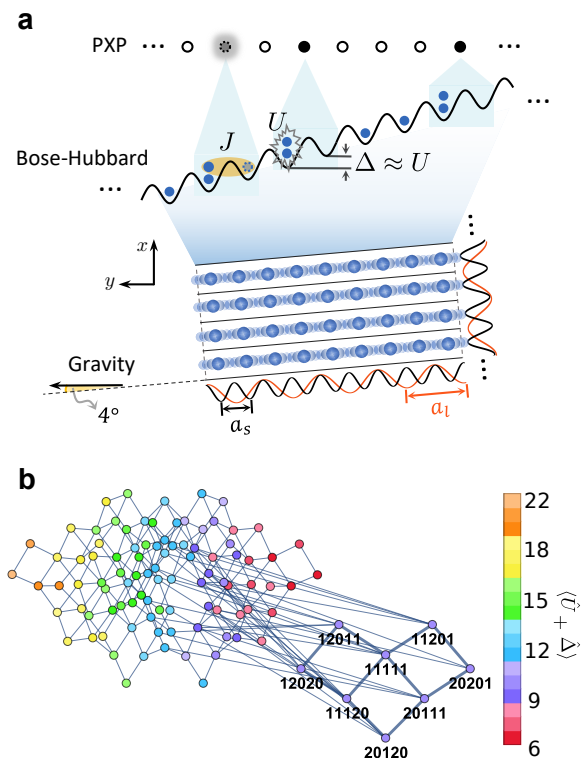

Figure 1. **Realizing the PXP model in a Bose–Hubbard quantum simulator.** **(a)** A schematic of the optical lattice. Deep lattice potential in the x-direction forms isolated chains in the y-direction, where the linear tilting potential is applied. Spin-dependent superlattices consisting of two standing waves in each direction can be individually controlled for state preparation and measurement. At the resonance $U \approx \Delta \gg J$, the dominant hopping process is $11 \leftrightarrow 20$. The PXP excitations, $\bullet$, live on the bonds between the lattice sites. The doublon configuration 20 in the Bose–Hubbard model maps to an excitation in the PXP model, while all other configurations are mapped to an empty site, $\circ$. For example, the given state $|\dots\circ\bullet\circ\bullet\circ\circ\circ\bullet\dots\rangle$ maps to the Fock state $|\dots120201120\dots\rangle$. **(b)** Emergence of the PXP subspace in the Bose–Hubbard model at the resonance $U \approx \Delta \gg J$. Dots represent Fock states of the tilted Bose–Hubbard model with 5 bosons on 5 sites (restricting to at most three bosons on any site). Lines denote the allowed hopping processes. The color scale shows the sum of interaction and tilt energies $\langle \hat{U} + \hat{\Delta} \rangle$ for each Fock state, and this value is conserved by resonant processes. The PXP dynamical subspace and its Fock states are explicitly labeled.

Our experiment begins with a $^{87}\mathrm{Rb}$ Bose-Einstein condensate, which is compressed in the z-direction and loaded into a single layer of pancake-shaped trap. We then perform superfluid to Mott insulator phase transition with optical lattices in the $x-y$ plane. In both x and y-direction, we have a superlattice that is formed by super-imposing the "short" lattice, with $a_s = 383.5$ nm spacing, and the "long" lattice, with $a_l = 767$ nm

spacing [34, 35], each can be individually controlled. We realize independent 1D Bose-Hubbard systems in the y-direction by ramping up short lattice depth in the x-direction over $40E_r$, with $E_r=h^2/8ma_s^2$ the short-lattice recoil energy, where h is the Planck constant and m is the ^{87}Rb atomic mass. The short lattice in the y-direction makes an approximately $4°$ angle with gravity, which results in a static linear tilt per site of $\Delta_g=816$ Hz, see Fig. 1**a**. An external magnetic field gradient Δ_B may be further added to create a tunable linear tilting potential $\Delta=\Delta_g+\Delta_B$. The effective Hamiltonian describing our simulator is

$$\hat{H} = -J\sum_{i=1}^{L-1}\left(\hat{b}_i^\dagger\hat{b}_{i+1}+\hat{b}_{i+1}^\dagger\hat{b}_i\right)+\hat{U}+\hat{\Delta}, \qquad (2)$$

where J is the hopping amplitude, $\hat{b}$, $\hat{b}^\dagger$ are the standard Bose annihilation and creation operators, the interaction energy is $\hat{U} = (U/2)\sum_{i=1}^L \hat{n}_i(\hat{n}_i-1)$, and tilt potential is $\hat{\Delta}=\Delta\sum_{i=1}^L i\hat{n}_i$. L denotes the number of sites in the chain with open boundary conditions and we restrict to the total filling equal to 1, i.e., with the same number of bosons as lattice sites.

In order to realize the PXP model in the Bose–Hubbard quantum simulator, we tune the parameters to the resonant regime $U\approx\Delta\gg J$ [36, 37], which has been studied extensively in the context of quantum Ising chains [38–40]. In this regime, three-boson occupancy of any site is strongly suppressed, and doublons can only be created by moving a particle to the left, e.g., $\ldots11\ldots\to\ldots20\ldots$, or destroyed by moving a particle to the right. The states of the PXP model are understood to live on the bonds of the Bose–Hubbard model. An excitation in the PXP model $\bullet_{j,j+1}$, living on the bond $(j,j+1)$, corresponds to the creation of a doublon 2_j0_{j+1} on site j in the Bose–Hubbard chain. We identify the unit-filling state $|111\ldots\rangle$ with the PXP polarized state, $|0\rangle$. Any other configuration of the PXP model can be mapped to a Fock state in the Bose–Hubbard model by starting from the unit-filling, identifying the bonds that carry PXP excitations and replacing the corresponding sites in the Mott state with $11\to20$. Applying this rule across the chain allows to map any basis state of the PXP model to a corresponding Fock state in the Bose–Hubbard model, e.g., the $|\mathbb{Z}_2\rangle$ state maps to the Fock state $|\ldots2020\ldots\rangle$. Fig. 1**b** illustrates the profound change in the connectivity of the Fock space near the resonance $U\approx\Delta\gg J$, with en emergent dynamical subspace isomorphic to the PXP model in the sector containing the $|\mathbb{Z}_2\rangle$ state. For a detailed derivation of the mapping, see Appendix A.

III. OBSERVATION OF $\mathbb{Z}_2$ QUANTUM MANY-BODY SCARS

To prepare the initial states, we first employ a entropy redistribution cooling method [34] with the superlattice in the y-direction to prepare a $\bar{n}=2$ Mott insulator in the left (odd) sites, while removing all atoms on the right (even) sites via site-dependent addressing [35]. This gives us the initial state $|\psi_0\rangle=|\mathbb{Z}_2\rangle=|2020\ldots\rangle$ (see Appendix B). In the region of interest, we have prepared 50 copies of the initial state $|\psi_0\rangle$ isolated by the short lattice along the x-direction. Each copy extends over 50 short lattice sites along the y-direction.

We quench the system out of equilibrium by abruptly dropping the y-lattice depth to $11.6E_r$, which corresponds to switching J from 0 to 51(1) Hz. This is done while simultaneously adjusting the lattice depth in the x and z-directions accordingly, such that the interaction strength matches the linear tilt with $U=\Delta=\Delta_g\approx16J$. After evolution time t, we freeze the dynamics by ramping up the y-lattice depth rapidly, and read out the atomic density on the left ($\langle\hat{n}_{\text{Left}}\rangle$) and right ($\langle\hat{n}_{\text{Right}}\rangle$) sites of the double-wells formed by the y-superlattice successively [35, 41]. This provides access to density imbalance, $\langle\hat{M}_z\rangle = (\langle\hat{n}_{\text{Left}}\rangle-\langle\hat{n}_{\text{Right}}\rangle)/(\langle\hat{n}_{\text{Left}}\rangle+\langle\hat{n}_{\text{Right}}\rangle)$, an observable corresponding to the staggered magnetization in the PXP model, see Fig. 2**a**. Another observable is the density of excitations in the PXP model, which is measured by projecting out the even atomic number occupancy on each site, then reading out the average odd particle density $\langle\hat{P}_{\hat{n}\in\text{odd}}\rangle_{(1)}$ [41]. Due to highly suppressed multi-boson occupancy, we have $\langle\hat{P}_{|\bullet\rangle}\rangle = \langle\hat{n}_{\text{doublon}}\rangle_{(1)}\approx(1-\langle\hat{P}_{\hat{n}\in\text{odd}}\rangle_{(1)})/2$.

Away from the resonance, the dynamics is ergodic and the staggered magnetization present in the initial $|\mathbb{Z}_2\rangle$ state quickly decays with time, see Fig. 2**b**. In contrast, by tuning to the vicinity of the resonance, $\Delta=U$, we observe distinct signatures of scarring: the system approximately undergoes persistent oscillations between the $|\mathbb{Z}_2\rangle \equiv |\bullet\circ\bullet\circ\ldots\rangle$ configuration and its partner shifted by one site, $|\bar{\mathbb{Z}}_2\rangle \equiv |\circ\bullet\circ\bullet\ldots\rangle$, as can be seen in the staggered magnetization profile and the density of excitations in Fig. 2**b**. The density of excitations does not distinguish between $|\mathbb{Z}_2\rangle$ and $|\bar{\mathbb{Z}}_2\rangle$ states, hence there is a trivial factor of 2 difference between the oscillation frequencies of $\langle\hat{P}_{|\bullet\rangle}\rangle$ and $\langle\hat{M}_z\rangle$.

The scarred oscillations in Fig. 2**b** are visibly damped with a decay time $\tau = 49.6 \pm 0.8$ ms. Nevertheless, as shown in Ref. [10], by periodically driving the system it is possible to 'refocus' the spreading of the many-body wavefunction in the Hilbert space and thereby enhance the scarring effect, as we demonstrate numerically in Fig. 2**c** and experimentally in Fig. 2**d**. Our driving protocol is based on modulating the laser intensity of the z-lattice, which translates into periodic modulation of the interaction energy, $U(t) = \Delta + U_0 + U_m\cos(\omega t)$, while Δ is kept fixed. This results in a modulation of the density of doublons in the chain, acting as the analog of the chemical potential in the PXP model.

Numerical simulations of the PXP model with the driven chemical potential, shown in Fig. 2**c**, demonstrate the dynamical stabilization of the Hilbert space trajec-
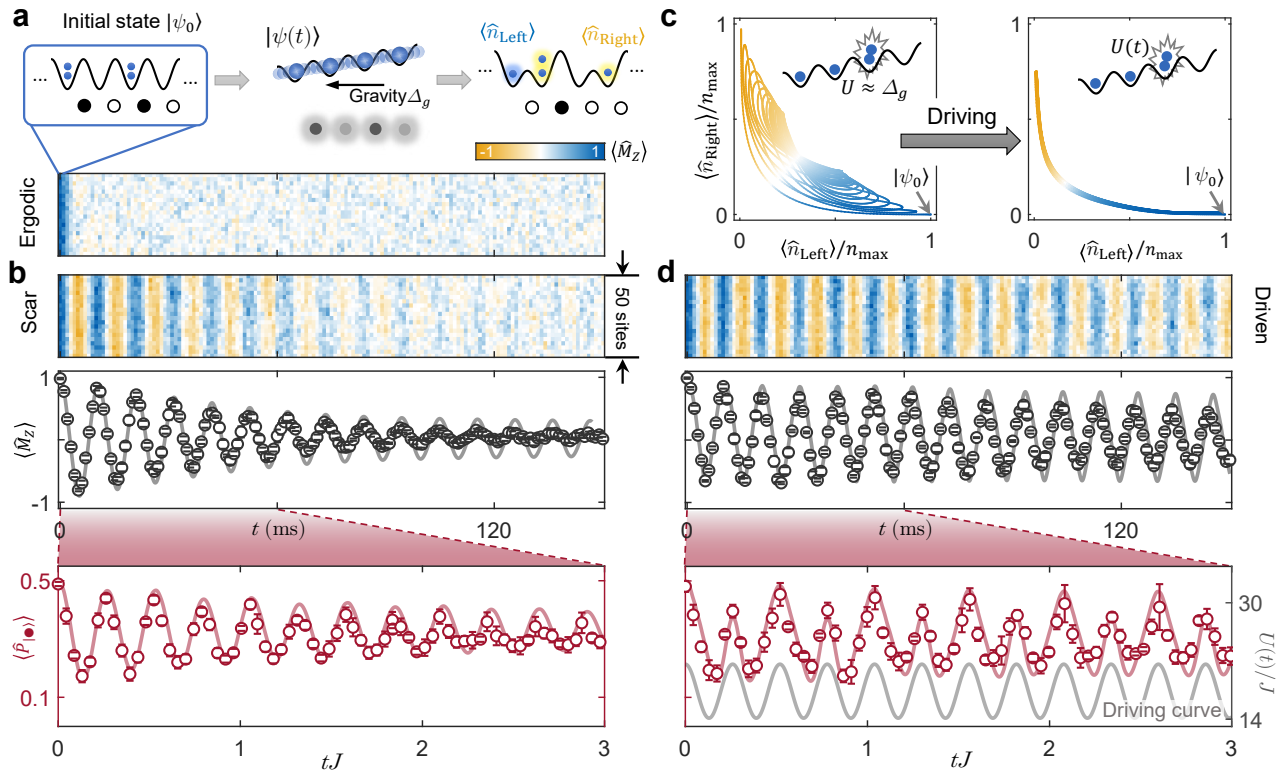
Figure 2. **Observation of $\mathbb{Z}_2$ quantum many-body scars in a Bose–Hubbard quantum simulator**. **(a)** Starting from the state $|\psi_0\rangle = |\ldots 2020\ldots\rangle$ – the analog of $|\mathbb{Z}_2\rangle$ state in the PXP model – we utilize gravity to provide linear tilt $\Delta = \Delta_g$. We characterize quench dynamics by measuring density imbalance and the number of doublons, corresponding to staggered magnetization $\langle \hat{M}_z \rangle$ and density of excitations $\langle \hat{P}_{|\bullet\rangle} \rangle$ in the PXP model. In the detuned regime $\Delta - U \approx -2J$, the dynamics is ergodic and the system has no memory of the initial state at late times. **(b)**: Tuning to $U \approx \Delta$, we observe persistent oscillations in both $\langle \hat{M}_z \rangle$ and $\langle \hat{P}_{|\bullet\rangle} \rangle$. This memory of the initial state is a signature of weak ergodicity breaking due to quantum many-body scars. **(c)**, **(d)**: Periodic modulation of the interaction $U(t) = \Delta + U_0 + U_m \cos(\omega t)$ with $U_0 = 1.85J$, $U_m = 3.71J$, $\omega = 3.85J$ leads to an enhancement of scarring. Panel **(c)** shows the numerically computed trajectory in the sublattice occupation plane for the PXP model with $N = 24$ sites, with and without driving. The sublattice occupancies $\langle \hat{n}_{\text{Left}} \rangle$, $\langle \hat{n}_{\text{Right}} \rangle$ are normalized to interval the [0,1]. The driving is seen to strongly suppress the spreading of the trajectory. **d**: Experimental measurements on the driven Bose-Hubbard model show robust scarred oscillations at all accessible times. In both the static and driven case, experimental data for $\langle \hat{M}_z \rangle$ and $\langle \hat{P}_{|\bullet\rangle} \rangle$ are in excellent agreement with TEBD numerical simulations shown by gray and red solid lines. Gray line in the lowest panel shows the modulation $U(t)$.

tory. We visualize the trajectory by plotting the average sublattice occupations, $\langle \hat{n}_{\text{Left}} \rangle$ and $\langle \hat{n}_{\text{Right}} \rangle$, normalized to the interval [0,1]. The $|\mathbb{Z}_2\rangle$ and $|\bar{\mathbb{Z}}_2\rangle$ states are located at the coordinates (1,0) and (0,1), which are the lower right and upper left corners of this diagram, respectively. The polarized state $|0\rangle$ is at the origin (0,0).

In the undriven case [left panel of Fig. 2**c**], the trajectory at first oscillates between $|\mathbb{Z}_2\rangle$ and $|\bar{\mathbb{Z}}_2\rangle$ states, while passing through a region with a lower number of excitations. However, as the time passes, the trajectory drifts, exploring progressively larger parts of the Hilbert space. By contrast, when the driving is turned on [right panel of Fig. 2**c**], the trajectory approximately repeats the first revival period of the undriven case, even at late times. Thus, the driving stabilized the scarred revivals without significantly altering their period.

Experimental measurements on the driven Bose-Hubbard model in Fig. 2**d** find a strong enhancement

of the amplitude of the oscillations in staggered magnetization with the decay time τ increasing to 208 ± 10 ms, while the period remains nearly the same as in the static case. Optimal driving parameters were determined numerically using a combination of simulated annealing and brute force search, see Supplementary Material [42].

We note that the experimental measurement of $\langle \hat{M}_z \rangle$ damps slightly faster than the theory prediction, shown by a line in Fig. 2**b**, at late times ($t>60$ ms). We attribute this to an inherent residual inhomogeneity across the lattice, which results in dephasing between different parts of the system, as well as possible decoherence induced by scattering of the lattice lasers. To avoid the effect of these undesired dephasing or decoherence effects, in the following we limit our investigation up to 60 ms.

IV. UNRAVELING THE DETAILS OF SCARRED DYNAMICS VIA QUANTUM INTERFERENCE

Entanglement entropy is key for characterizing scarring behavior. Entropy provides a window into the evolution of the system's wave function and the spreading of quantum entanglement. For a system trapped in a scarred subspace, thermalization is inhibited and the system exhibits suppressed entropy growth and periodic fidelity revivals. Measuring these observables usually requires brute-force state tomography, but for our 50-site Bose–Hubbard system with a Hilbert space dimension exceeding 10^{28}, this approach is generally impossible.

However, the superlattice in the x-direction allows us to probe entanglement entropy by interfering identical copies in the double wells, analogous to the $50:50$ beam splitter (BS) interference employed in photonics experiments [43]; see Fig. 3a. This is done by freezing the dynamics along the chains in the y-direction after evolution time t, then we interfere copies of $|\psi(t)\rangle$ in the double wells formed by the x-superlattice (see Appendix C). After the interference, a parity projection helps read out the average odd particle density $\langle \hat{P}^{\mathrm{BS}}_{\hat{n}\in\mathrm{odd}}\rangle_{(1)}$, which gives us access to the second-order Rényi entropy [44]. We measure the entropy of single-site subsystems $S_{(1)} = -\ln(\mathrm{Tr}_{(1)}[\hat{\rho}(t)^2]) = -\ln(1 - 2\langle \hat{P}^{\mathrm{BS}}_{\hat{n}\in\mathrm{odd}}\rangle_{(1)})$, where $\hat{\rho}(t) = |\psi(t)\rangle\langle\psi(t)|$ is the density matrix. Entanglement entropy $S_{(1)}$, shown in Fig. 3b, grows much more slowly than expected in a thermalizing system. The growth is accompanied by oscillations with the same frequency as $\langle \hat{P}_{|\bullet}\rangle$ in Fig. 2b, implying that the system returns to the neighborhood of product states $|\mathbb{Z}_2\rangle$ and $|\bar{\mathbb{Z}}_2\rangle$. Furthermore, the entropy growth becomes almost fully suppressed by periodic driving, indicating that the scarred subspace disconnects from the thermalizing bulk of the spectrum. Numerical TEBD simulations confirm that this lack of thermalization at the single-site level provides a good approximation for the behavior of larger subsystems, as demonstrated by the half-chain bipartite entropy $S_{L/2}$ plotted in Fig. 3b. This shows that scarring traps the system in a vanishingly small corner of an exponentially large Hilbert space.

V. EMERGENCE OF DETUNED SCARRING IN THE POLARIZED STATE

Up to this point, we have provided extensive benchmarks of our quantum simulator against the previously known case of $\mathbb{Z}_2$ quantum many-body scars [9]. In this section we demonstrate that our quantum simulator also hosts distinct scarring regimes for initial states other than $|\mathbb{Z}_2\rangle$, which are enabled by detuning and further stabilized by periodic drive. We highlight this finding by observation of scarring behavior in the polarized state $|0\rangle$, previously not associated with scars.

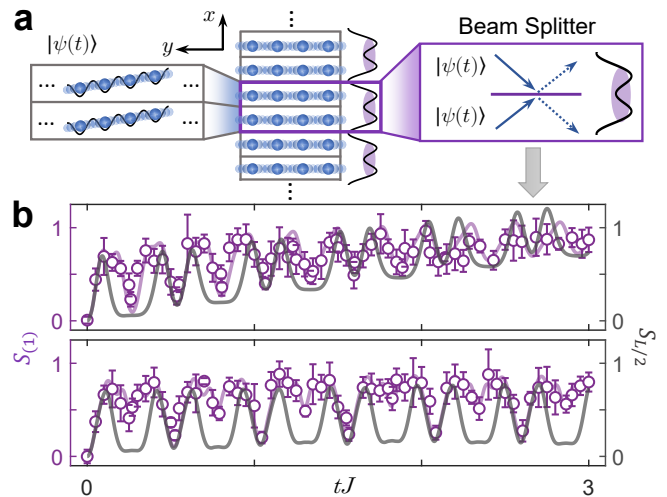We first prepare the unit-filling state $|1111\ldots\rangle$ by

Figure 3. **Probing many-body scarred dynamics via quantum interference.** (a) After evolution time t, we freeze the dynamics in the y-direction, then by interfering two identical copies in the double wells along the x-direction, we obtain the second order Rényi entropy. (b) The entropy for a single site, $S_{(1)}$, is seen to have robust oscillations with the same frequency as in Fig. 2b, indicating a lack of thermalization. The slow growth of entropy in the absence of driving (upper panel) is strongly suppressed when we drive the system using the same parameters as in Fig. 2d (lower panel). In both cases, the single-site entropy is a good approximation to the half-chain entropy, $S_{L/2}$, evaluated numerically using TEBD (grey line).

transferring $|2,0\rangle$ to $|1,1\rangle$ states in the superlattice [34], which maps to the polarized state in the PXP model (see also Appendix B). In the absence of detuning or periodic drive, we observe fast relaxation: the density of excitations, single-site entropy, and fidelity all rapidly relax, with no visible oscillations beyond the timescale $\sim 1/J$, see Fig. 4a. Interestingly, when we bias the system by a static detuning, $U_0 = -2.38J$, we observe the emergence of oscillations in all three observables, accompanied by a slight decay, see Fig. 4b. Finally, if we also periodically modulate the interaction with amplitude $U_m = 1.54J$ and frequency $\omega = 4.9J\times 2\pi$, we find a dramatic enhancement of scarring, Fig. 4c. In particular, both entropy and fidelity now show pronounced oscillations, signaling robust scar-induced coherence at all experimentally-accessible times.

The intuitive picture behind our observations is summarized as follows. In the absence of detuning or periodic drive, the system initialized in the polarized state undergoes chaotic dynamics and rapidly explores the entire Hilbert space. By biasing the system via static detuning, thermalization can be suppressed over moderate timescales. Finally, by periodically driving the system it is possible to 'refocus' the spreading of the many-body wavefunction in the Hilbert space and thereby enhance the scarring effect, similar to the findings of Ref. [10]
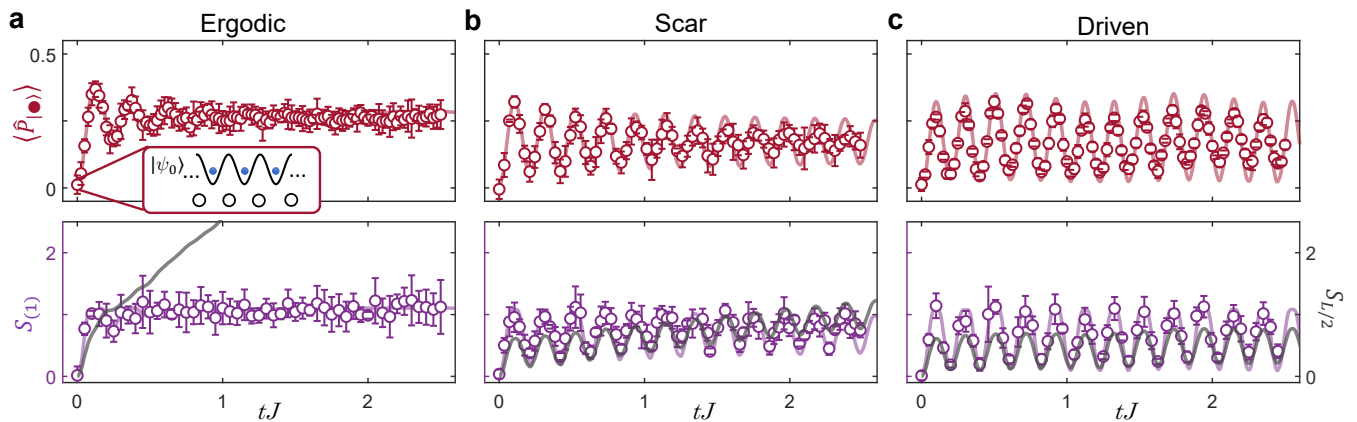
Figure 4. **Emergence of many-body scarring in the polarized state**. **a**: Fast thermalization from the unit-filling state in the Bose–Hubbard chain at $U=\Delta$ resonance. **b**: Emergence of scarred dynamics in the presence of static detuning. **c**: Dynamical stabilization of scarred dynamics in the presence of both detuning and periodic driving. Top and bottom row show the experimental measurements of the density of excitations and second Rényi entropy, respectively. The ergodic case shows fast growth of the half-chain entropy compared to the single-site entropy, while for the scarred dynamics, the single-site entropy approximates well the half-chain entropy, with or without periodic driving. Static detuning is $U_0=-2.38J$ and the modulation parameters are $U_m=1.54J$, $\omega=4.9J\times2\pi$. Lines are the results of TEBD simulations.

for the $|\mathbb{Z}_2\rangle$ state. In the remainder of this section, we present our theoretical analysis of the experiment that supports this interpretation of the dynamics.

Fig. 5 shows the results of exact diagonalizations of the PXP model in Eq. (1) in the presence of static detuning, $\hat{H}(\mu) = \hat{H}_{\mathrm{PXP}} + \mu_0 \sum_i \hat{n}_i$, where $\hat{n}_i$ takes the value equal to 1 if site i contains an excitation and 0 otherwise. The static chemical potential μ_0 is proportional to the Bose-Hubbard detuning parameter U_0 in Fig. 4. Fig. 5a plots the overlap of all energy eigenstates $|E\rangle$ of the pure PXP model ($\mu_0 = 0$) with the polarized state $|\psi_0\rangle = |0\rangle$. As expected, we do not see any hallmarks of scars, such as ergodicity-violating eigenstates with anomalously enhanced projection on $|0\rangle$. Moreover, the lowest entropy eigenstates, denoted by squares in Fig. 5b, are the known $\mathbb{Z}_2$ scarred eigenstates [31] which are hidden in the bulk of spectrum when the overlap is taken with the $|0\rangle$ state.

On the other hand, when we add the static chemical potential $\mu_0 = 1.68\Omega$, corresponding to the detuning value in Fig. 4, a band of scarred eigenstates with anomalously large overlap with $|0\rangle$ emerges; see Fig. 5c. The band of scarred eigenstates, highlighted by star symbols in Fig. 5c, spans the entire energy spectrum, but their support on $|0\rangle$ is biased towards the ground state due to the breaking of particle-hole symmetry by detuning. The detuned scarred states also have anomalously low entanglement entropy, as seen in Fig. 5d.

A few comments are in order. We note that exact diagonalization confirms that the PXP model remains chaotic for the value of detuning used in Fig. 5c, and this detuning is not large enough to trivially fragment the entire spectrum into disconnected sectors with the given numbers of excitations [42]. Moreover, we confirmed that the scarred eigenstates in Fig. 5c are distinct from the

ones associated with the $|\mathbb{Z}_2\rangle$ state in Fig. 5a. Thus, it remains to be understood if these eigenstates can be described within the su(2) spectrum-generating algebra framework developed for the $|\mathbb{Z}_2\rangle$ state in Ref. [45].

Nevertheless, similar to the $|\mathbb{Z}_2\rangle$ case, the scarring from the $|0\rangle$ state can be further enhanced by periodic modulation of the PXP chemical potential, $\mu(t) = \mu_0 + \mu_m \cos(\omega t)$. By evaluating the corresponding Floquet operator, we find that a single Floquet mode develops a very large overlap with the $|0\rangle$ state [42]. The existence of a single Floquet mode, whose mixing with other modes is strongly suppressed, gives rise to robust oscillations in the dynamics well beyond the experimentally accessible timescales.

To probe the ergodicity of the dynamics from the polarized state, we compare the difference between the predictions of the diagonal and canonical ensembles for an observable such as the average number of excitations, see Fig. 6a. These two ensembles are expected to give the same result if strong Eigenstate Thermalization Hypothesis (ETH) holds [46] and all eigenstates at a similar energy density yield the same expectation value for local observables. Fig. 6 (a) shows the discrepancy between the two ensembles is the strongest around $\mu_0 \approx 1.68\Omega$, where we observe strong scarring. For μ_0/Ω close to 0, the polarized state thermalizes quickly towards the thermal value expected for a state whose expectation value of the energy is near the middle of the many-body spectrum. For very large μ_0/Ω, we enter a trivial regime where the polarized state is close to the ground state and only a few eigenstates at low energies are relevant for the dynamics. Hence, in this regime, quenching from the polarized state is similar to quenching from a thermal state at a very low temperature and the agreement between the two ensem-
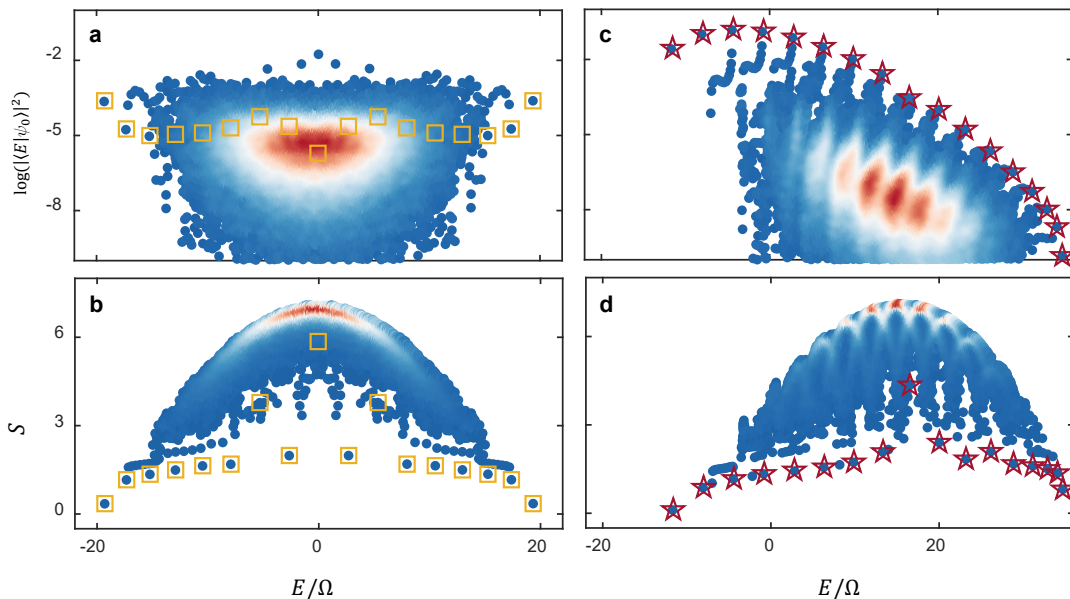
Figure 5. **Eigenstate properties of the detuned PXP model**. **a**: Overlaps of all eigenstates of the PXP model with the polarized state $|\psi_0\rangle = |0\rangle$. **b**: Bipartite entanglement entropy of the eigenstates in panel **a**. The squares mark the previously known $\mathbb{Z}_2$ scarred eigenstates. **c**, **d**: Same as panels **a**, **b** but for the PXP model with the static chemical potential $\mu_0 = 1.68\Omega$, approximately corresponding to the experimental value of detuning in Fig. 4. The stars denote the detuned scar eigenstates, which have high overlap with $|0\rangle$ state as well as low entropy. All data is obtained by exact diagonalization of the PXP model on a ring with $N=32$ sites in the zero-momentum and inversion-symmetric sector.

bles is again very good. However, in this regime, only a very small part of the many-body Hilbert space is explored by the dynamics. This is not the case the scarred regime that we investigate experimentally, and this can be demonstrated by studying the relevant classical limit, as shown next.

In the single-particle case, scarred quantum dynamics originates from an unstable periodic orbit in the classical limit $\hbar \to 0$ [47]. In a many-body system, one approach to establishing a quantum-classical correspondence is to project the Schrödinger dynamics into a variational manifold, e.g., spanned by matrix product states [48] – a method known as the "time-dependent variational principle" (TDVP). It was shown that the scarred dynamics of the $|\mathbb{Z}_2\rangle$ state in the PXP model is well-captured by the TDVP approach, allowing to identify a classical orbit [16]. In Figs. 6b-c we utilize the TDVP approach to gain semiclassical understanding of the detuned scarred dynamics from the $|0\rangle$ state. We parametrize the TDVP manifold using translation-invariant, spin-coherent states compatible with the Rydberg blockade constraint [49]. The states are defined by the Bloch sphere angles θ and ϕ, where $\sin(\theta)$ is proportional to the density of excitations, while ϕ describes the phase. In the thermodynamic limit, we can obtain classical equations of motion for θ, ϕ (see Ref. [50] for a detailed derivation). Fig. 6b demonstrates that this classical dynamical system provides an excellent approximation of the quantum trajectory for sufficiently large values of μ_0, including $\mu_0=1.68\Omega$.

To quantify the accuracy of the TDVP approach in

capturing the quantum dynamics, we use "quantum leakage" – the instantaneous norm of a component of the state vector that lies outside the TDVP manifold, $\gamma^2 \equiv (1/N)||\,|\dot{\psi}\rangle - i\hat{H}\,|\psi\rangle\,||^2$ [16]. For the initial state $|0\rangle$, the leakage has a simple analytic expression $\gamma^2 = \Omega^2 \sin^6\theta/(1+\sin^2\theta)$ [50]. The leakage is higher as θ is increased, corresponding to a larger density of excitations. In this regime, i.e., for small values of μ_0/Ω, the PXP constraint has a strong effect and the spin-coherent state ansatz does not faithfully capture the dynamics. On the other hand, for large values of μ_0/Ω, the leakage is low but θ is confined to values near zero, thus the trajectory does not explore much of the Hilbert space. This corresponds to the trivial case where the dynamics is confined to very low densities of excitations, rendering the constraint unimportant. Finally, in the intermediate regime of μ_0/Ω where we observe the scarring, the TDVP dynamics is able to "avoid" the high-leakage area, as seen in Fig. 6c, while at the same time θ is not pinned to zero and the dynamics is not confined to one corner of the Hilbert space.

VI. DISCUSSION AND OUTLOOK

We performed a quantum simulation of the paradigmatic PXP model of many-body scarring using a tilted Bose–Hubbard optical lattice. We demonstrated the existence of persistent quantum revivals from the $|\mathbb{Z}_2\rangle$ initial state and their dynamical stabilization, opening up
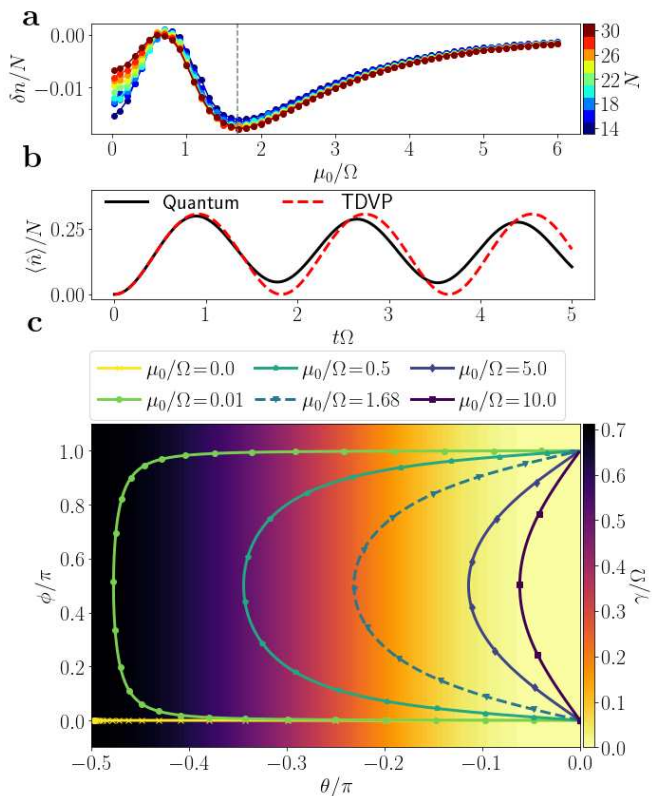
Figure 6. **Non-ergodic dynamics from the polarized state in the detuned PXP model**. **a**: Difference between the expectation values of the diagonal and canonical ensembles for the average number of excitations. The discrepancy is maximized around $\mu_0/\Omega \approx 1.68$. **b**: Average number of excitations at $\mu_0/\Omega = 1.68$ following the quench from $|0\rangle$ state shows good agreement between exact quantum dynamics and TDVP approximation. Exact dynamics is for system size $N = 32$ spins. **c**: Trajectory in the TDVP manifold for different values of μ_0/Ω. Color scale denotes quantum leakage γ, defined in the text, which bounds the accuracy of the TDVP approximation. The markers are spaced in time by $\Delta t = 0.15/\Omega$. For the optimal value $\mu_0 = 1.68\Omega$, identified in panel **a** and also used in experiment, the trajectory avoids the high-leakage region and approximates well the quantum dynamics, while it is not limited to a small corner of the many-body Hilbert space.

a new route for the investigation of scarring beyond Rydberg atom arrays. By harnessing the effect of detuning, we observed a previously unknown scarring regime associated with the polarized initial state. As the latter state is spatially homogeneous, its preparation does not require a superlattice, which makes further investigations of scarring phenomena accessible to a large class of ultracold atom experiments.

Moreover, we have demonstrated that periodic driving can lead to a striking decoupling of the scarred subspace from the rest of the thermalizing bulk of the spectrum, as revealed by the arrested growth of entanglement entropy. The mechanism of this enhancement is a subject of on-

going investigations. On the one hand, Ref. [51] used a kicked toy model to argue that the scarring enhancement originates from a discrete time crystalline order. On the other hand, Ref. [52] studied the cosine drive employed in experiment, finding two distinct regimes with long-lived scarred revivals. In the regime corresponding to the parameter values in Fig. 2 above, the driving parameters need to be fine-tuned to match the intrinsic revival frequency of the undriven scarred system. Moreover, the stabilization was no longer possible when the system was perturbed by terms which destroy scarring in the undriven case. This suggests that driving indeed acts as an enhancement mechanism, preventing dynamics from "leaking" into the thermalizing bulk.

Our demonstration of scarring in the $|0\rangle$ state highlights the importance of energy density. While the $|\mathbb{Z}_2\rangle$ state has predominant support on the eigenstates in the middle of the spectrum, i.e., it constitutes an "infinite temperature" ensemble, the support of the $|0\rangle$ state is biased towards one end of the spectrum as result of particle-hole symmetry breaking via the detuning potential. This suggests that, depending on the effective temperature, one can realize scarring from a much larger class of initial states with a suitable choice of detuning and periodic driving protocols. We illustrate this in Appendix D by simulating the quench of the chemical potential in the PXP model (see also Ref. [50]).

The versatility of optical lattice platforms allows to directly probe the link between many-body scarring and other forms of ergodicity-breaking phenomena, such as Hilbert space fragmentation and disorder-free localization, as the latter can be conveniently studied in our setup by varying the tilt. In this context, we note that Ref. [12] has recently used the tilt potential to demonstrate Hilbert space fragmentation in the Fermi-Hubbard optical lattice. By contrast, in this work we explored ergodicity breaking due to many-body scars occurring within a *single* fragment of the Hilbert space. While many-body scarring can be induced in the Fermi-Hubbard model by tuning to a similar resonance condition [53], the underlying mechanism is an approximate dimerization of the chain, which is conceptually different from the PXP-type scarring considered here.

In future work, it would be interesting to explore realizations of new scarring models by tuning to other resonance conditions and other types of lattices, including ladders and two-dimensional arrays. Indeed, it is known that the U(1) quantum link model (QLM) [54, 55] can be exactly mapped to the PXP model [56]. As such, recent large-scale experiments realizing the U(1) QLM [57, 58] can in principle also probe our results. A proposal has recently been introduced to extend these setups to $2+1$D [59], where a mapping between the U(1) QLM and PXP model does not hold, which would allow probing how the scarring regimes discovered in this work would behave in higher spatial dimensions. Finally, the observation of long-lived quantum coherence due to scarring and its controllable enhancement via periodic modulation, lays the

foundation for applications such as quantum memories and quantum sensing [60, 61].

Appendix A: Mapping the tilted 1D Bose-Hubbard onto the PXP model at $\Delta \approx U$ resonance

The Hamiltonian describing our 1D Bose-Hubbard model is given in Eq. (2) of the main text, with J denoting the hopping amplitude, $\hat{H}_U$ the corresponding interaction term, $\hat{H}_\Delta$ the tilt potential. We denote by L the number of lattice sites and assume open boundary conditions (OBC). Unless specified otherwise, we fix the filling factor to $\nu = 1$, i.e., the number of bosons is equal to the number of sites in the chain.

In the $U, \Delta \gg J$ limit, the energy spectrum of the Hamiltonian in Eq. (2) splits into bands with approximately constant expectation value of the diagonal terms, $\langle \hat{H}_U + \hat{H}_\Delta \rangle \approx \text{const}$, and the Hilbert space becomes fragmented. At the $U \approx \Delta \gg J$ resonance, the only process which conserves $\langle \hat{H}_U + \hat{H}_\Delta \rangle$ is 11 ↔ 20, i.e. doublons can only be created by moving a particle to the left and destroyed by moving a particle to the right. In the connected component of the Fock state $|111 \ldots 111\rangle$, the system in the resonant regime is described by an effective Hamiltonian

$$\hat{H}_{\text{eff}} = -J \sum_{i=1}^{L-1} \left(\hat{b}_i^\dagger \hat{b}_{i+1} \hat{n}_i (2-\hat{n}_i) \hat{n}_{i+1}(2-\hat{n}_{i+1}) + \text{h.c.} \right),$$
(A1)

which results from the first-order Schrieffer-Wolff transformation applied to Eq. (2) [62]. In Supplementary Material [42] we discuss the effect of higher-order terms in the Schrieffer-Wolff transformation.

In the remainder of this appendix, we show that the Hamiltonian (A1) is equivalent to the PXP Hamiltonian [27, 28] (see also Ref. [36] for the original derivation of the mapping and a recent review [37]). The connected component of the Hilbert space contains only certain types of two-site configurations (20, 11, 12, 02, 01), while all other two-site configurations are forbidden (22, 21, 10, 00). If we consider the configuration 20 to be an excitation, all allowed configurations can be mapped to those of the PXP model as follows:

$$\begin{aligned}
\ldots 20 \ldots &\leftrightarrow \circ \bullet \circ \\
\ldots 11 \ldots &\leftrightarrow \circ \circ \circ \\
\ldots 12 \ldots &\leftrightarrow \circ \circ \bullet \\
\ldots 02 \ldots &\leftrightarrow \bullet \circ \bullet \\
\ldots 01 \ldots &\leftrightarrow \bullet \circ \circ
\end{aligned}$$
(A2)

Note that excitations live on the bonds between sites and this mapping also includes links to the two surrounding sites. For example, the configuration $\ldots 2020 \ldots$ maps to $\circ \bullet \circ \bullet \circ$ and not to $\circ \bullet \circ \circ \bullet \circ$. On the other hand, the configuration 2020 with OBCs on both sides maps to $\bullet \circ \bullet$, as there are no bonds across the boundaries.

The effective Hamiltonian (A1) can be rewritten as:

$$\hat{H}_{\text{eff}} = -J \sum_{i=1}^{L-1} \left(\underbrace{\hat{b}_i^\dagger \hat{b}_{i+1} \delta_{\hat{n}_i,1} \delta_{\hat{n}_{i+1},1}}_{\sqrt{2}\hat{P}_{j-1}\hat{\sigma}_j^+ \hat{P}_{j+1}} + \underbrace{\hat{b}_{i+1}^\dagger \hat{b}_i \delta_{\hat{n}_i,2} \delta_{\hat{n}_{i+1},0}}_{\sqrt{2}\hat{P}_{j-1}\hat{\sigma}_j^- \hat{P}_{j+1}} \right).$$
(A3)

In this equation, the index i labels the sites, while j labels the bonds between sites. The Kronecker delta functions have been expressed in terms of projectors, $\hat{P}_j = |\circ_j\rangle\langle\circ_j|$, and the bosonic hopping terms correspond to the spin raising and lowering operators, $\hat{\sigma}_j^\pm$, on the bond j. We can use delta functions because there are no configurations with more than 2 particles per site in this connected component and the only possible values of $\hat{n}_i(2-\hat{n}_i)$ are 0 and 1. Moving a particle to the neighboring site on the left corresponds to creating an excitation, moving to the right to annihilating, while delta functions act as constraints.

Finally, the effective Hamiltonian is equivalent to the PXP Hamiltonian

$$\begin{aligned}
\hat{H}_{\text{PXP}} &= \Omega \sum_{j=1}^{N} \left(\hat{P}_{j-1} \hat{\sigma}_j^+ \hat{P}_{j+1} + \hat{P}_{j-1} \hat{\sigma}_j^- \hat{P}_{j+1} \right) \\
&= \Omega \sum_{j=1}^{N} \hat{P}_{j-1} \hat{X}_j \hat{P}_{j+1},
\end{aligned}$$
(A4)

when we set $\Omega = -\sqrt{2}J$ and $N = L - 1$, with $\hat{X}_j \equiv |\circ_j\rangle\langle\bullet_j| + |\bullet_j\rangle\langle\circ_j|$ denoting the usual Pauli x matrix. In case of OBCs, the two boundary terms become $\hat{X}_1 \hat{P}_2$ and $\hat{P}_{N-1}\hat{X}_N$. Note that the effective bosonic model in Eq. (A3) for a system size L is equivalent to the PXP

model for size $N = L - 1$ since the number of bonds is the number of sites minus one.

In the PXP model, the initial states which lead to pronounced quantum revivals are the two states with the maximal number of excitations – the Néel states, $|\bullet\circ\bullet\circ\ldots\bullet\circ\rangle$ and $|\circ\bullet\circ\bullet\ldots\circ\bullet\rangle$ [23, 31]. The equivalent states in the tilted Bose-Hubbard model are $|2020\ldots201\rangle$ and $|12020\ldots20\rangle$, for odd system sizes, and $|2020\ldots20\rangle$ and $|120\ldots201\rangle$ for even sizes. In our experimental setup, it is not possible to exactly prepare the $|2020\ldots201\rangle$ state due to the inability to independently control single sites. Instead, our experiment realizes the $|2020\ldots20\rangle$ state, which corresponds to the Néel state $|\bullet\circ\bullet\circ\ldots\bullet\circ\bullet\rangle$ in the PXP model with an odd number of sites and OBCs.

Fig. 7 numerically demonstrates the mapping between the tilted Bose-Hubbard model in Eq. (2) and the PXP model in Eq. (1) in a lattice size $L = 9$. The figure shows the the overlap of eigenstates with the Néel state as a function of energy, for the choice of parameters $U=\Delta=12$ and $J = 1$. The energy spectrum is split into bands with approximately constant expectation value of the sum of interaction and tilt terms $\langle \hat{H}_U + \hat{H}_\Delta \rangle$, as indicated by different colors. The inset shows the top part of the highest-overlap band, around the energy $E = \langle 202020201|\hat{H}|202020201\rangle = 432$. This band is described by the effective Hamiltonian (A1), which preserves the expectation value $\langle \hat{H}_U + \hat{H}_\Delta \rangle$ and is equivalent to the PXP Hamiltonian. A band of scarred eigenstates is magnified in the inset, and indeed resembles similar plots for the PXP model [31]. As the two Néel states have the maximal number of doublons at filling factor $\nu = 1$, this type of dynamics also leads to oscillations in doublon number, which was experimentally measured in Fig. 2.

Appendix B: State preparation and detection

Our experiment starts out with a two-dimensional Bose–Einstein condensate of ^{87}Rb atoms prapared in the hyperfine state $|\downarrow\rangle = 5S_{1/2}\,|F=1, m_F=-1\rangle$. By applying a microwave pulse, atoms can be adiabatically transferred to the state $|\uparrow\rangle = 5S_{1/2}\,|F=2, m_F=-2\rangle$, which is resonant with the imaging laser and thus can be detected. The atoms are initially confined to a single layer of a pancake-shaped trap with 3 μm period. In both x and y-directions, we have an optical superlattice that can be controlled separately. Each superlattice potential is generated by super-imposing two standing waves with laser frequency λ_s=767 nm and λ_l=1534 nm, which can be described by

$$V(x) = V_s^x \cos^2(kx) - V_l^x \cos^2(kx/2 + \theta_x)$$
$$V(y) = V_s^y \cos^2(ky) - V_l^y \cos^2(ky/2 + \theta_y), \quad \text{(B1)}$$

where $V_{s(l)}^{x(y)}$ is the depth of short (long) lattice in $x(y)$-direction, $k=2\pi/\lambda_s$ is the short lattice wave number, and
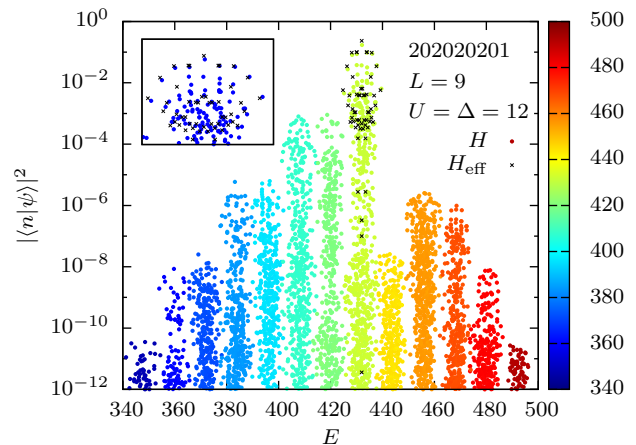

Figure 7. **Numerical demonstration of the mapping between the PXP and tilted Bose-Hubbard models.** Overlap of the state $|202020201\rangle$ with the eigenstates of the tilted Bose-Hubbard model in Eq. (2) for $J = 1$ and $U = \Delta = 12$ (in units $\hbar = 1$). The color indicates the expectation value of the diagonal part of the Hamiltonian, $\langle \hat{H}_U + \hat{H}_\Delta \rangle$, for each eigenstate. The black crosses correspond to the effective model in Eq. (A3), shifted by the energy $E = \langle 202020201|\hat{H}|202020201\rangle = 432$. The inset shows the top part of band with the highest overlap, where a band of scarred eigenstates analogous to that in the PXP model can be seen.

$\theta_{x(y)}$ the relative phase between the short and long lattices in $x(y)$-direction.

We first perform a cooling technique by loading the atoms into a staggered superlattice in the y-direction at $\theta_y=\pi/4$, meanwhile ramping up only the short lattice in the x-direction. We tune the y-superlattice potential to create a Mott insulator with $\bar{n}$=2 filling in odd sites, while even sites form a $\bar{n}$=1.5 superfluid, serving as a reservoir for carrying away the thermal entropy [34].

Atoms in even sites are removed by performing site-selective addressing. This is done by first setting θ_y=0 to form double wells, then tuning the polarization of the short lattice laser along the y-direction to create an energy splitting between even and odd sites for the $|\downarrow\rangle$ to $|\uparrow\rangle$ transition. We transfer the atoms in even sites to $|\uparrow\rangle$ and remove them with the imaging laser [35]. This way we have prepared the initial $|\mathbb{Z}_2\rangle$ state $|2020\ldots\rangle$. The same site-selective addressing procedure is also utilized to read out atomic density on even and odd sites separately in experiment. Inside each isolated double-well unit, we can perform state engineering that transfers the state $|2, 0\rangle$ to $|1, 1\rangle$ [34]. This results in the unit-filling state $|1111\ldots\rangle$ which corresponds to the polarized state $|0\rangle$ in the PXP model.
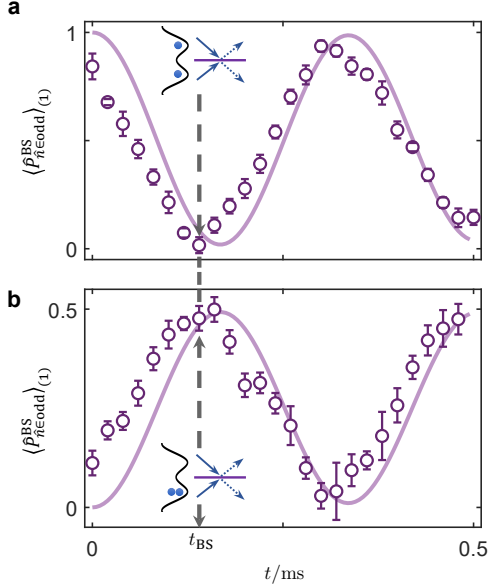
Figure 8. **Quantum interference.** **(a)** Interfering $|1,1\rangle$ product states in the double wells. **(b)** Interfering $|2,0\rangle$ product states in the double wells. Solid lines are TEBD simulations. Experimental data is shifted forward at earliest times due to the 50 μs ramping time of the lattice potential.

Appendix C: Quantum interference in the double wells

The beam splitter (BS) interference is realized in the balanced double wells formed by the superlattices in the x-direction, expressed in Eq. (B1) by setting $\theta_x=0$. In the non-interacting limit, indistinguishable bosonic particles coming into the the interference at $t=0$ interfere according to the bosonic bunching. Therefore, equal number of atoms coming into the two ports at $t=0$ results in $\langle \hat{P}^{\text{BS}}_{\hat{n}\in\text{odd}}\rangle=0$ at t_{BS}, while different number of atoms interfering results in $\langle \hat{P}^{\text{BS}}_{\hat{n}\in\text{odd}}\rangle=0.5$. Each copy of atoms coming into the interference is prepared individually, hence no global phase between them, resulting in the equivalence between the two output ports [44].

To implement the quantum interference protocol, we quench the x-lattice potentials to $V_s^x=6E_r$ and $V_l^x=5E_r$, resulting in the intra-double-well tunneling at $J\approx740$ Hz and inter-double-well tunneling $J'\approx35$ Hz. Simultaneously, we lower the lattice depth in the x-direction to $25E_r$ and trapping frequency in the z-direction to 1.4 kHz, achieving an interaction of $U\approx360$ Hz. Two examples are shown here in Fig. 8, where we interfere product states $|1,1\rangle$ (Fig. 8**a**) or $|2,0\rangle$ (Fig. 8**b**) in the double wells and read out the average odd particle density. At $t_{\text{BS}}=0.14$ ms we identify the beam splitter operation, where $|1,1\rangle$ gives $\langle \hat{P}^{\text{BS}}_{\hat{n}\in\text{odd}}\rangle_{(1)}=0.01(3)$, while $|2,0\rangle$ gives $\langle \hat{P}^{\text{BS}}_{\hat{n}\in\text{odd}}\rangle_{(1)}=0.48(3)$. We simulate the interference dynamics with a 20-site chain consisting of 10 double-well units. We find good agreement at later times, while the

earlier times are affected by the finite time in the lowering and rising of lattice potentials, which takes 50 μs. The finite interaction strength and inter-double-well tunneling results in about 1% error in the beam splitter operation in the simulation, but this is beyond the precision of our absorption imaging.
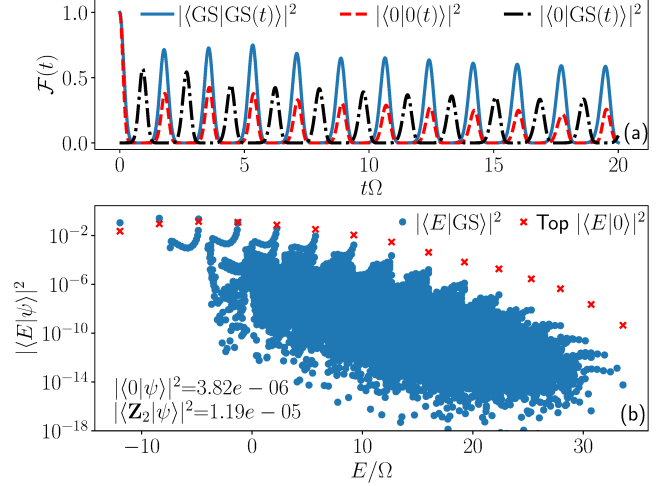

Figure 9. **Emergence of many-body scarring by quenching the chemical potential in the PXP model from $\mu_i = -0.76\Omega$ to $\mu_f = 1.6\Omega$.** Top panel: The dynamics of quantum fidelity (blue solid line) is similar to that of the polarized state for the same value of μ_f (red dashed line). The overlap between the time-evolved state and $|0\rangle$ (black dash-dotted line) shows a significant state transfer occurs between them. Bottom panel: The overlap of the pre-quench ground state with the eigenstates of $\hat{H}(\mu_f)$ displays characteristic scar tower structures. Red crosses denote the highest overlaps with $|0\rangle$ state in each scarred tower. The overlap of the pre-quench ground state with $|0\rangle$ and $|\mathbb{Z}_2\rangle$ states is quoted in the inset. All data is for $N=32$ spins in the zero-momentum, inversion-symmetric sector of the Hilbert space.

Appendix D: Other scarred states

In addition to the $|\mathbb{Z}_2\rangle$ and $|0\rangle$ state, we find other reviving states in the PXP model with static detuning, $\hat{H}(\mu)$, introduced in Sec. V. These initial states are the ground states of $\hat{H}(\mu_i)$ and they exhibit revivals when the detuning is quenched to a different value, $\hat{H}(\mu_i) \to \hat{H}(\mu_f)$. This setup generalizes the quench protocols studied in the main text. For example, setting $\mu_i\to-\infty$, the pre-quench ground state is simply the $|\mathbb{Z}_2\rangle$ state and then quenching to $\mu_f=0$ (pure PXP model) gives rise to scarred many-body revivals. Conversely, if we set $\mu_i\to\infty$, the ground state is $|0\rangle$ and quenching to $\mu_f=1.68\Omega$ also leads to scarring, as this value corresponds to the Bose-Hubbard detuning value in Fig. 4.

We numerically identify similar scarring phenomenology in a larger set of initial conditions by varying the parameters μ_i and μ_f. In Fig. 9 we present an illustrative

example for $\mu_\mathrm{i}=-0.76\Omega$ and $\mu_\mathrm{f}=1.6\Omega$. Unlike the $|\mathbb{Z}_2\rangle$ and $|0\rangle$ states, the ground state of $\hat{H}(\mu_\mathrm{i})$, for general values of $|\mu_\mathrm{i}| < 2$, is not a product state. Nevertheless, such ground states have low entanglement entropy and can be prepared experimentally, while at the same time they are nearly orthogonal to $|\mathbb{Z}_2\rangle$ and $|0\rangle$ states (the overlap with the latter is on the order 10^{-5}). We emphasize that this does not require fine tuning – we find large regions of μ_i and μ_f leading to scarring.

The dynamics in Fig. 9 is similar to that of the polarized state evolved with $\hat{H}(\mu=1.68\Omega)$. During the evolution, the state periodically transfers to the polarized state and then returns to itself. The frequency of revivals is approximately the same as that for the polarized state evolved with the same static detuning μ_f, but the revivals are more prominent. The overlap of the $\hat{H}(\mu_\mathrm{i})$ ground state with all the eigenstates of $\hat{H}(\mu_\mathrm{f})$ is shown in the bottom panel of Fig. 9. These overlaps exhibit a similar pattern with the overlap of eigenstates with the polarized states (red crosses). Furthermore, the atypical eigenstates appear to be the same in the two cases, up to a difference in phase. This is similar to what we find for the $|\mathbb{Z}_2\rangle$ and $|\bar{\mathbb{Z}}_2\rangle$ state at $\mu_\mathrm{f}=0$: both states have the same magnitude of the overlap with each eigenstate, while the phases are different.

[1] J. M. Deutsch, "Quantum statistical mechanics in a closed system," Phys. Rev. A **43**, 2046 (1991).
[2] Mark Srednicki, "Chaos and quantum thermalization," Phys. Rev. E **50**, 888 (1994).
[3] Marcos Rigol, Vanja Dunjko, and Maxim Olshanii, "Thermalization and its mechanism for generic isolated quantum systems," Nature **452**, 854–858 (2008).
[4] Toshiya Kinoshita, Trevor Wenger, and David S. Weiss, "A quantum Newton's cradle," Nature **440**, 900–903 (2006).
[5] Rahul Nandkishore and David A. Huse, "Many-body localization and thermalization in quantum statistical mechanics," Annual Review of Condensed Matter Physics **6**, 15–38 (2015).
[6] Dmitry A. Abanin, Ehud Altman, Immanuel Bloch, and Maksym Serbyn, "Colloquium: Many-body localization, thermalization, and entanglement," Rev. Mod. Phys. **91**, 021001 (2019).
[7] Maksym Serbyn, Dmitry A Abanin, and Zlatko Papić, "Quantum many-body scars and weak breaking of ergodicity," Nature Physics **17**, 675–685 (2021).
[8] Sanjay Moudgalya, B. Andrei Bernevig, and Nicolas Regnault, "Quantum many-body scars and hilbert space fragmentation: A review of exact results," arXiv e-Prints (2021), arXiv:2109.00548 [cond-mat.str-el].
[9] Hannes Bernien, Sylvain Schwartz, Alexander Keesling, Harry Levine, Ahmed Omran, Hannes Pichler, Soonwon Choi, Alexander S. Zibrov, Manuel Endres, Markus Greiner, Vladan Vuletić, and Mikhail D. Lukin, "Probing many-body dynamics on a 51-atom quantum simulator," Nature **551**, 579–584 (2017).
[10] D. Bluvstein, A. Omran, H. Levine, A. Keesling, G. Semeghini, S. Ebadi, T. T. Wang, A. A. Michailidis, N. Maskara, W. W. Ho, S. Choi, M. Serbyn, M. Greiner, V. Vuletić, and M. D. Lukin, "Controlling quantum many-body dynamics in driven rydberg atom arrays," Science **371**, 1355–1359 (2021).
[11] Wil Kao, Kuan-Yu Li, Kuan-Yu Lin, Sarang Gopalakrishnan, and Benjamin L. Lev, "Topological pumping of a 1d dipolar gas into strongly correlated prethermal states," Science **371**, 296–300 (2021).
[12] Sebastian Scherg, Thomas Kohlert, Pablo Sala, Frank Pollmann, Bharath Hebbe Madhusudhana, Immanuel Bloch, and Monika Aidelsburger, "Observing non-ergodicity due to kinetic constraints in tilted fermi-hubbard chains," Nature Communications **12**, 4490 (2021).
[13] Paul Niklas Jepsen, Yoo Kyung Lee, Hanzhen Lin, Ivana Dimitrova, Yair Margalit, Wen Wei Ho, and Wolfgang Ketterle, "Catching Bethe phantoms and quantum many-body scars: Long-lived spin-helix states in Heisenberg magnets," (2021), arXiv:2110.12043 [cond-mat.quant-gas].
[14] Sanjay Moudgalya, Nicolas Regnault, and B. Andrei Bernevig, "Entanglement of exact excited states of Affleck-Kennedy-Lieb-Tasaki models: Exact results, many-body scars, and violation of the strong eigenstate thermalization hypothesis," Phys. Rev. B **98**, 235156 (2018).
[15] Naoto Shiraishi and Takashi Mori, "Systematic construction of counterexamples to the eigenstate thermalization hypothesis," Phys. Rev. Lett. **119**, 030601 (2017).
[16] Wen Wei Ho, Soonwon Choi, Hannes Pichler, and Mikhail D. Lukin, "Periodic orbits, entanglement, and quantum many-body scars in constrained models: Matrix product state approach," Phys. Rev. Lett. **122**, 040603 (2019).
[17] Daniel K. Mark, Cheng-Ju Lin, and Olexei I. Motrunich, "Unified structure for exact towers of scar states in the Affleck-Kennedy-Lieb-Tasaki and other models," Phys. Rev. B **101**, 195131 (2020).
[18] Sho Sugiura, Tomotaka Kuwahara, and Keiji Saito, "Many-body scar state intrinsic to periodically driven system," Phys. Rev. Research **3**, L012010 (2021).
[19] Kaoru Mizuta, Kazuaki Takasan, and Norio Kawakami, "Exact Floquet quantum many-body scars under Rydberg blockade," Phys. Rev. Research **2**, 033284 (2020).
[20] Bhaskar Mukherjee, Sourav Nandy, Arnab Sen, Diptiman Sen, and K. Sengupta, "Collapse and revival of quantum many-body scars via Floquet engineering," Phys. Rev. B **101**, 245107 (2020).
[21] Ian Mondragon-Shem, Maxim G. Vavilov, and Ivar Martin, "Fate of quantum many-body scars in the presence of disorder," PRX Quantum **2**, 030349 (2021).
[22] Naoyuki Shibata, Nobuyuki Yoshioka, and Hosho Katsura, "Onsager's scars in disordered spin chains," Phys. Rev. Lett. **124**, 180604 (2020).
[23] C. J. Turner, A. A. Michailidis, D. A. Abanin, M. Serbyn, and Z. Papić, "Weak ergodicity breaking from quantum many-body scars," Nature Physics **14**, 745–749 (2018).

[24] Cheng-Ju Lin and Olexei I. Motrunich, "Exact quantum many-body scar states in the Rydberg-blockaded atom chain," Phys. Rev. Lett. **122**, 173401 (2019).

[25] Thomas Iadecola, Michael Schecter, and Shenglong Xu, "Quantum many-body scars from magnon condensation," Phys. Rev. B **100**, 184312 (2019).

[26] Vedika Khemani, Chris R. Laumann, and Anushya Chandran, "Signatures of integrability in the dynamics of Rydberg-blockaded chains," Phys. Rev. B **99**, 161101 (2019).

[27] Paul Fendley, K. Sengupta, and Subir Sachdev, "Competing density-wave orders in a one-dimensional hard-boson model," Phys. Rev. B **69**, 075106 (2004).

[28] Igor Lesanovsky and Hosho Katsura, "Interacting Fibonacci anyons in a Rydberg gas," Phys. Rev. A **86**, 041601 (2012).

[29] B. Sun and F. Robicheaux, "Numerical study of two-body correlation in a 1d lattice with perfect blockade," New Journal of Physics **10**, 045032 (2008).

[30] B. Olmos, M. Müller, and I. Lesanovsky, "Thermalization of a strongly interacting 1d Rydberg lattice gas," New Journal of Physics **12**, 013024 (2010).

[31] C. J. Turner, A. A. Michailidis, D. A. Abanin, M. Serbyn, and Z. Papić, "Quantum scarred eigenstates in a Rydberg atom chain: Entanglement, breakdown of thermalization, and stability to perturbations," Phys. Rev. B **98**, 155134 (2018).

[32] Eric J. Heller, "Bound-state eigenfunctions of classically chaotic hamiltonian systems: Scars of periodic orbits," Phys. Rev. Lett. **53**, 1515–1518 (1984).

[33] C. J. Turner, J.-Y. Desaules, K. Bull, and Z. Papić, "Correspondence principle for many-body scars in ultracold rydberg atoms," Phys. Rev. X **11**, 021021 (2021).

[34] Bing Yang, Hui Sun, Chun-Jiong Huang, Han-Yi Wang, Youjin Deng, Han-Ning Dai, Zhen-Sheng Yuan, and Jian-Wei Pan, "Cooling and entangling ultracold atoms in optical lattices," Science **369**, 550–553 (2020).

[35] Bing Yang, Han-Ning Dai, Hui Sun, Andreas Reingruber, Zhen-Sheng Yuan, and Jian-Wei Pan, "Spin-dependent optical superlattice," Phys. Rev. A **96**, 011602 (2017).

[36] Subir Sachdev, K. Sengupta, and S. M. Girvin, "Mott insulators in strong electric fields," Phys. Rev. B **66**, 075128 (2002).

[37] K. Sengupta, "Phases and dynamics of ultracold bosons in a tilted optical lattice," arXiv e-Prints (2021), arXiv:2109.02657 [cond-mat.quant-gas].

[38] F. Meinert, M. J. Mark, E. Kirilov, K. Lauber, P. Weinmann, A. J. Daley, and H.-C. Nägerl, "Quantum quench in an atomic one-dimensional ising chain," Phys. Rev. Lett. **111**, 053003 (2013).

[39] Florian Meinert, Manfred J. Mark, Emil Kirilov, Katharina Lauber, Philipp Weinmann, Michael Gröbner, Andrew J. Daley, and Hanns-Christoph Nägerl, "Observation of many-body dynamics in long-range tunneling after a quantum quench," Science **344**, 1259–1262 (2014).

[40] Jonathan Simon, Waseem S. Bakr, Ruichao Ma, M. Eric Tai, Philipp M. Preiss, and Markus Greiner, "Quantum simulation of antiferromagnetic spin chains in an optical lattice," Nature **472**, 307–312 (2011).

[41] Bing Yang, Hui Sun, Robert Ott, Han-Yi Wang, Torsten V. Zache, Jad C. Halimeh, Zhen-Sheng Yuan, Philipp Hauke, and Jian-Wei Pan, "Observation of gauge invariance in a 71-site bose–hubbard quantum simulator," Nature **587**, 392–396 (2020).

[42] Supplemental Online material containing additional results and background calculations supporting the results in this work. The SOM contains references [1, 2, 9, 10, 23, 31, 51, 56, 62–69].

[43] Adam M. Kaufman, Malte C. Tichy, Florian Mintert, Ana Maria Rey, and Cindy A. Regal, *Advances in Atomic, Molecular and Optical Physics*, 1st ed., Vol. 67 (Elsevier Inc., 2018) pp. 377–427, arXiv:1801.04670.

[44] Rajibul Islam, Ruichao Ma, Philipp M. Preiss, M. Eric Tai, Alexander Lukin, Matthew Rispoli, and Markus Greiner, "Measuring entanglement entropy in a quantum many-body system," Nature **528**, 77–83 (2015).

[45] Soonwon Choi, Christopher J. Turner, Hannes Pichler, Wen Wei Ho, Alexios A. Michailidis, Zlatko Papić, Maksym Serbyn, Mikhail D. Lukin, and Dmitry A. Abanin, "Emergent su(2) dynamics and perfect quantum many-body scars," Phys. Rev. Lett. **122**, 220603 (2019).

[46] Luca D'Alessio, Yariv Kafri, Anatoli Polkovnikov, and Marcos Rigol, "From quantum chaos and eigenstate thermalization to statistical mechanics and thermodynamics," Adv. Phys. **65**, 239 (2016).

[47] E. J. Heller, "Wavepacket dynamics and quantum chaology," in *Chaos and quantum physics*, Vol. 52 (North-Holland: Amsterdam, 1991).

[48] Jutho Haegeman, J. Ignacio Cirac, Tobias J. Osborne, Iztok Pižorn, Henri Verschelde, and Frank Verstraete, "Time-dependent variational principle for quantum lattices," Phys. Rev. Lett. **107**, 070601 (2011).

[49] A. A. Michailidis, C. J. Turner, Z. Papić, D. A. Abanin, and M. Serbyn, "Slow quantum thermalization and many-body revivals from mixed phase space," Phys. Rev. X **10**, 011055 (2020).

[50] Aiden Daniel, Andrew Hallam, Jean-Yves Desaules, Ana Hudomal, Guo-Xian Su, Jad C. Halimeh, and Zlatko Papić, "Bridging quantum criticality via many-body scarring," arXiv e-Prints (2023), arXiv:2301.03631.

[51] N. Maskara, A. A. Michailidis, W. W. Ho, D. Bluvstein, S. Choi, M. D. Lukin, and M. Serbyn, "Discrete time-crystalline order enabled by quantum many-body scars: Entanglement steering via periodic driving," Phys. Rev. Lett. **127**, 090602 (2021).

[52] Ana Hudomal, Jean-Yves Desaules, Bhaskar Mukherjee, Guo-Xian Su, Jad C. Halimeh, and Zlatko Papić, "Driving quantum many-body scars in the pxp model," Phys. Rev. B **106**, 104302 (2022).

[53] Jean-Yves Desaules, Ana Hudomal, Christopher J. Turner, and Zlatko Papić, "Proposal for realizing quantum scars in the tilted 1d fermi-hubbard model," Phys. Rev. Lett. **126**, 210601 (2021).

[54] S Chandrasekharan and U.-J Wiese, "Quantum link models: A discrete approach to gauge theories," Nuclear Physics B **492**, 455 – 471 (1997).

[55] U.-J. Wiese, "Ultracold quantum gases and lattice systems: quantum simulation of lattice gauge theories," Annalen der Physik **525**, 777–796 (2013).

[56] Federica M. Surace, Paolo P. Mazza, Giuliano Giudici, Alessio Lerose, Andrea Gambassi, and Marcello Dalmonte, "Lattice gauge theories and string dynamics in rydberg atom quantum simulators," Phys. Rev. X **10**, 021041 (2020).

[57] Zhi-Cheng Yang, Fangli Liu, Alexey V. Gorshkov, and Thomas Iadecola, "Hilbert-space fragmentation from strict confinement," Phys. Rev. Lett. **124**, 207602 (2020).

[58] Zhao-Yu Zhou, Guo-Xian Su, Jad C. Halimeh, Robert

Ott, Hui Sun, Philipp Hauke, Bing Yang, Zhen-Sheng Yuan, Jürgen Berges, and Jian-Wei Pan, "Thermalization dynamics of a gauge theory on a quantum simulator," Science **377**, 311–314 (2022).

[59] Jesse Osborne, Ian P. McCulloch, Bing Yang, Philipp Hauke, and Jad C. Halimeh, "Large-scale 2 + 1D U(1) gauge theory with dynamical matter in a cold-atom quantum simulator," arXiv e-Prints (2022), arXiv:2211.01380.

[60] Shane Dooley, "Robust quantum sensing in strongly interacting systems with many-body scars," PRX Quantum **2**, 020330 (2021).

[61] Jean-Yves Desaules, Francesca Pietracaprina, Zlatko Papić, John Goold, and Silvia Pappalardi, "Extensive multipartite entanglement from su(2) quantum many-body scars," Phys. Rev. Lett. **129**, 020601 (2022).

[62] Sergey Bravyi, David P DiVincenzo, and Daniel Loss, "Schrieffer–wolff transformation for quantum many-body systems," Ann. Phys. **326**, 2793–2826 (2011).

[63] Jad C. Halimeh, Robert Ott, Ian P. McCulloch, Bing Yang, and Philipp Hauke, "Robustness of gauge-invariant dynamics against defects in ultracold-atom gauge theories," Phys. Rev. Research **2**, 033361 (2020).

[64] Bhaskar Mukherjee, Arnab Sen, Diptiman Sen, and K. Sengupta, "Dynamics of the vacuum state in a periodically driven rydberg chain," Phys. Rev. B **102**, 075123 (2020).

[65] Zhiyuan Yao, Lei Pan, Shang Liu, and Hui Zhai, "Quantum many-body scars and quantum criticality," (2021), arXiv:2108.05113 [cond-mat.quant-gas].

[66] Vadim Oganesyan and David A. Huse, "Localization of interacting fermions at high temperature," Phys. Rev. B **75**, 155111 (2007).

[67] Vedika Khemani, Chris R. Laumann, and Anushya Chandran, "Signatures of integrability in the dynamics of rydberg-blockaded chains," Phys. Rev. B **99**, 161101 (2019).

[68] Guifré Vidal, "Efficient classical simulation of slightly entangled quantum computations," Phys. Rev. Lett. **91**, 147902 (2003).

[69] Johannes Hauschild and Frank Pollmann, "Efficient numerical simulations with Tensor Networks: Tensor Network Python (TeNPy)," SciPost Phys. Lect. Notes , 5 (2018), code available from https://github.com/tenpy/tenpy, arXiv:1805.00055.

Supplementary Material for "Observation of many-body scarring in a Bose-Hubbard quantum simulator"

Guo-Xian Su,[1,2,3] Hui Sun,[1,2,3] Ana Hudomal,[4,5] Jean-Yves Desaules,[4] Zhao-Yu Zhou,[1,2,3]
Bing Yang,[6] Jad C. Halimeh,[7] Zhen-Sheng Yuan,[1,2,3] Zlatko Papić,[4] and Jian-Wei Pan[1,2,3]

[1]*Department of Modern Physics, University of Science and Technology of China, Hefei, Anhui 230026, China*
[2]*Physikalisches Institut, Ruprecht-Karls-Universität Heidelberg,*
Im Neuenheimer Feld 226, 69120 Heidelberg, Germany
[3]*CAS Center for Excellence and Synergetic Innovation Center in Quantum Information and Quantum Physics,*
University of Science and Technology of China, Hefei, Anhui 230026, China
[4]*School of Physics and Astronomy, University of Leeds, Leeds LS2 9JT, UK*
[5]*Institute of Physics Belgrade, University of Belgrade, 11080 Belgrade, Serbia*
[6]*Department of Physics, Southern University of Science and Technology, Shenzhen, China*
[7]*INO-CNR BEC Center and Department of Physics,*
University of Trento, Via Sommarive 14, I-38123 Trento, Italy

CONTENTS

I. HIGHER ORDER TERMS IN THE MAPPING BETWEEN PXP AND BOSE-HUBBARD MODELS

The effective Hamiltonian at $U \approx \Delta$ resonance, derived in the main text:

$$\hat{H}_{\text{eff}} = -J \sum_{i=1}^{L-1} \left(\hat{b}_i^\dagger \hat{b}_{i+1} \hat{n}_i (2-\hat{n}_i) \hat{n}_{i+1} (2-\hat{n}_{i+1}) + \text{h.c.} \right). \tag{S1}$$

results from the first-order Schrieffer-Wolff transformation [1]. This effective Hamiltonian (S1) can be equiva-

lently written as:

$$\hat{H}_{\text{eff}} = -J \sum_{i=1}^{L-1} \left(\underbrace{\hat{b}_i^\dagger \hat{b}_{i+1} \delta_{\hat{n}_i,1} \delta_{\hat{n}_{i+1},1}}_{\sqrt{2}\hat{P}_{j-1}\hat{\sigma}_j^+\hat{P}_{j+1}} + \underbrace{\hat{b}_{i+1}^\dagger \hat{b}_i \delta_{\hat{n}_i,2} \delta_{\hat{n}_{i+1},0}}_{\sqrt{2}\hat{P}_{j-1}\hat{\sigma}_j^-\hat{P}_{j+1}} \right), \tag{S2}$$

which yields the PXP model at this order of the Schrieffer-Wolff transformation. In this section we look at the relevant terms that arise in the effective Hamiltonian at second order. To simplify the notation we write these terms as sums of range-3 operators, where $|111\rangle \langle 120|_j$ denotes the operator changing sites $j-1$, j and $j+1$ from 120 to 111 while leaving all other sites unaffected.

First, we can identify the matrix elements that take the system out of the PXP sector. This happens by the appearance of sites with 3 bosons via the operator

$$\hat{H}_{\text{out}} = \frac{\sqrt{3}J^2}{U} \sum_{j=2}^{L-1} \Big(|300\rangle \langle 201|_j + |201\rangle \langle 300|_j$$
$$+ 2|300\rangle \langle 120|_j + 2|120\rangle \langle 300|_j \Big). \tag{S3}$$

There are also off-diagonal matrix elements connecting states within the PXP sector, given by

$$\hat{H}_{\text{OD}} = \frac{2J^2}{U} \sum_{j=2}^{L-1} \Big(|120\rangle \langle 201|_j + |201\rangle \langle 120|_j \Big). \tag{S4}$$

There are also additional off-diagonal matrix elements connecting states outside of the PXP sector, but as they do not directly influence the dynamics out of it we do not describe them here.

Finally, the diagonal operator in this sector is given by

$$\hat{H}_{\text{Diag}} = \frac{J^2}{U} \sum_{j=2}^{L-1} \Big(4|120\rangle \langle 120|_j - |111\rangle \langle 111|_j$$
$$+ |020\rangle \langle 020|_j - |112\rangle \langle 112|_j \Big) \tag{S5}$$
$$+ \frac{J^2}{U} \Big(|01\rangle \langle 01|_{L-1} - |11\rangle \langle 11|_1 - |12\rangle \langle 12|_1 \Big),$$

where the two-site operator $|11\rangle\langle12|_j$ acts on sites j and $j+1$. As bulk terms get added, the overall diagonal factors are extensive in the system size in the Fock basis. The state with the lowest on-site potential is $|111\ldots11\rangle$ with a value of $-\frac{(L-1)J^2}{U}$. The maximum is $\approx\frac{4J^2L}{3U}$ for the state $|120120\ldots120\rangle$, which corresponds to the $\mathbb{Z}_3$ state in the PXP terminology.

In order to see how these second-order terms change the effective model we can rewrite Eqs. (S4)-(S5) for the PXP model with $N = L - 1$ sites. To do this we introduce the single-site projector on the excited state $\hat{Q}_j = |\bullet\rangle\langle\bullet| = \mathbf{1} - \hat{P}_j$. We then obtain

$$\hat{H}_{\mathrm{OD}}^{\mathrm{PXP}}=\frac{2J^2}{U}\sum_{j=1}^{N-2}\Big(\hat{P}_{j-1}\hat{\sigma}_j^+\hat{\sigma}_{j+1}^-\hat{P}_{j+2}+\hat{P}_{j-1}\hat{\sigma}_j^-\hat{\sigma}_{j+1}^+\hat{P}_{j+2}\Big)$$
$$+\frac{2J^2}{U}\left(\hat{\sigma}_1^+\hat{\sigma}_2^-\hat{P}_3+\hat{\sigma}_1^-\hat{\sigma}_2^+\hat{P}_3\right)$$
$$+\frac{2J^2}{U}\left(\hat{P}_{N-3}\hat{\sigma}_{N-1}^+\hat{\sigma}_N^-+\hat{P}_{N-2}\hat{\sigma}_{N-1}^-\hat{\sigma}_N^+\right)$$

$$(S6)$$

and

$$\hat{H}_{\mathrm{Diag}}^{\mathrm{PXP}}=\frac{J^2}{U}\sum_{j=1}^{N-2}\big(4\hat{P}_{j-1}\hat{P}_j\hat{Q}_{j+1}\hat{P}_{j+2}-\hat{P}_{j-1}\hat{P}_j\hat{P}_{j+1}\hat{P}_{j+2}$$
$$+\hat{Q}_{j-1}\hat{P}_j\hat{Q}_{j+1}\hat{P}_{j+2}-\hat{P}_{j-1}\hat{P}_j\hat{P}_{j+1}\hat{Q}_{j+2}\big)$$
$$+\frac{J^2}{U}\big(4\hat{P}_0\hat{Q}_1\hat{P}_2-\hat{P}_0\hat{P}_1\hat{P}_2-\hat{P}_0\hat{P}_1\hat{Q}_2$$
$$+4\hat{P}_{N-2}\hat{P}_{N-1}\hat{Q}_N-\hat{P}_{N-2}\hat{P}_{N-1}\hat{P}_N$$
$$+\hat{Q}_{N-2}\hat{P}_{N-1}\hat{Q}_N\big)$$
$$+\frac{J^2}{U}\left(\hat{Q}_{N-1}\hat{P}_N-\hat{P}_0\hat{P}_1-\hat{P}_0\hat{Q}_1\right),$$

$$(S7)$$

respectively. We notice that the off-diagonal correction has the form of a constrained XY term.

II. NUMERICAL DEMONSTRATIONS OF THE MAPPING BETWEEN PXP AND TILTED BOSE-HUBBARD MODEL

In this Section, we numerically corroborate the mapping between PXP and Bose-Hubbard models. We use exact diagonalization to demonstrate the consistency between dynamics and eigenstate properties in the PXP model and the Bose-Hubbard model tuned to the resonance $U=\Delta$. Unless specified otherwise, we restrict the occupancy of any site to be at maximum 3 bosons, as our results are found to be insensitive to allowing more than 3 bosons on any site. For numerical simulations, it is convenient to work in natural units $\hbar=1$. We adopt this convention for presenting all numerical results in this Supplementary Material.

In analogy with the PXP model, the Bose-Hubbard system initialized in the state $2020\ldots201$ is expected to oscillate between this state and the state $12020\ldots20$.

This is not only the case for the effective model (S2) which is exactly equivalent to PXP, but also for the full tilted Bose-Hubbard model at the $U = \Delta$ resonance, as can be observed in Fig. S1.
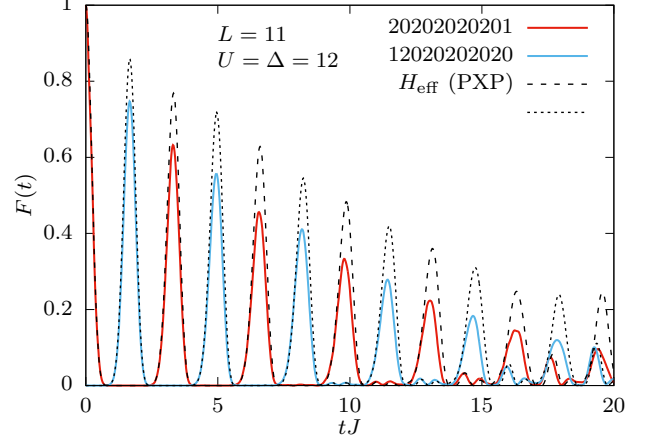

FIG. S1. Evolution of quantum fidelity $F(t) = |\langle\psi_0|e^{-iHt}|\psi_0\rangle|^2$ starting from the state $|\psi_0\rangle = |2020\ldots201\rangle$ (red) and the amplitude of state transfer, $\mathcal{O}(t) = |\langle\psi|e^{-iHt}|\psi_0\rangle|^2$, with the state $|\psi\rangle = |12020\ldots2020\rangle$ (blue). The evolution is governed by the full Bose-Hubbard Hamiltonian with $J=1$, $U=\Delta=12$ and maximally 3 bosons per site. The dashed and dotted black lines correspond to the effective model in Eq. (S2). System size $L=11$, filling factor $\nu=1$.
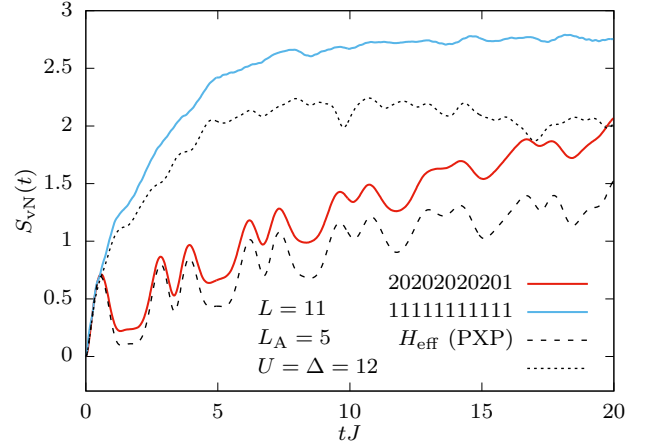

FIG. S2. Evolution of the bipartite entanglement entropy for the initial states $|2020\ldots201\rangle$ (red) and $|111\ldots111\rangle$ (blue). The evolution is governed by the full tilted Bose-Hubbard Hamiltonian with $J = 1$, $U = \Delta = 12$ and maximally 3 bosons per site. The dashed and dotted black lines correspond to the effective model from Eq. (S2). System size $L = 11$, subsystem $L_A = 5$, filling factor $\nu = 1$.

In Fig. S2 we show the evolution of the bipartite von Neumann entanglement entropy, $S_{\mathrm{vN}}(t) = -\mathrm{Tr}_A(\hat{\rho}_A\ln\hat{\rho}_A)$, where $\hat{\rho}_A$ is the reduced density matrix for subsystem A of length L_A. The system is initially prepared in the state $2020\ldots201$ or the completely homogeneous state $111\ldots111$. As in the PXP model, the

entanglement entropy for the 2020...201 state exhibits slow and approximately linear growth in time. In contrast, the entanglement entropy for the state 111...111 rapidly saturates, implying that the system quickly thermalizes.
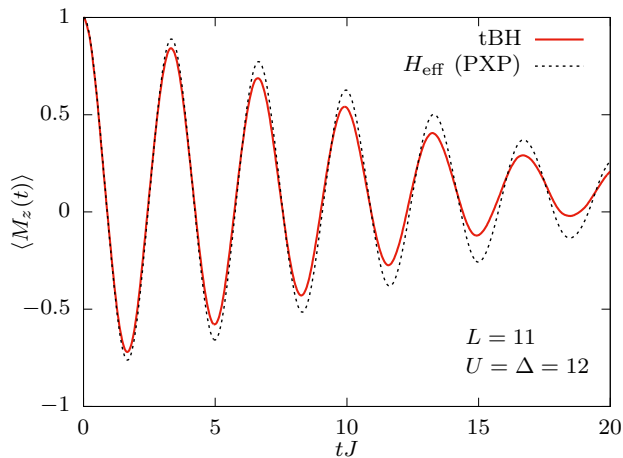

FIG. S3. Evolution of staggered magnetization $\langle \hat{M}_z \rangle = (\langle \hat{n}_{\mathrm{odd}} \rangle - \langle \hat{n}_{\mathrm{even}} \rangle)/(\langle \hat{n}_{\mathrm{odd}} \rangle + \langle \hat{n}_{\mathrm{even}} \rangle)$, where $\hat{n}_{\mathrm{odd}}$ and $\hat{n}_{\mathrm{even}}$ are the numbers of particles on odd and even sites. The evolution is governed by the full Bose-Hubbard Hamiltonian with $J = 1$ and $U = \Delta = 12$ (solid red line) and the effective model from Eq. (S2) which is equivalent to the PXP model (dashed black line). System size $L = 11$, filling factor $\nu = 1$, initial state $|2020\ldots201\rangle$.

The evolution of density imbalance between the even and odd sites $\langle \hat{M}_z \rangle = (\langle \hat{n}_{\mathrm{odd}} \rangle - \langle \hat{n}_{\mathrm{even}} \rangle)/(\langle \hat{n}_{\mathrm{odd}} \rangle + \langle \hat{n}_{\mathrm{even}} \rangle)$, which corresponds to staggered magnetization in the PXP model, is shown in Fig. S3. This is one of the quantities that was experimentally measured in the main text. Here we again compare the evolution with the full tilted Bose-Hubbard Hamiltonian and the effective Hamiltonian (S2), the latter being equivalent to the PXP model, and we find excellent agreement between the two.

As a side note, the system is also described by PXP-like effective models at other integer filling factors. The reviving initial states are of the form $|(n+1)(n-1)(n+1)(n-1)\ldots(n+1)(n-1)n\rangle$ for $\nu = n$, e.g. $|3131\ldots312\rangle$ for $\nu = 2$ and $|4242\ldots423\rangle$ for $\nu = 3$, as shown in Fig. S4. Revival frequency increases with n as $\sqrt{n(n-1)}$, but the revivals decay faster for larger n.

III. ALTERNATIVE MAPPING BETWEEN PXP AND TILTED 1D BOSE-HUBBARD WITH STAGGERED DETUNING

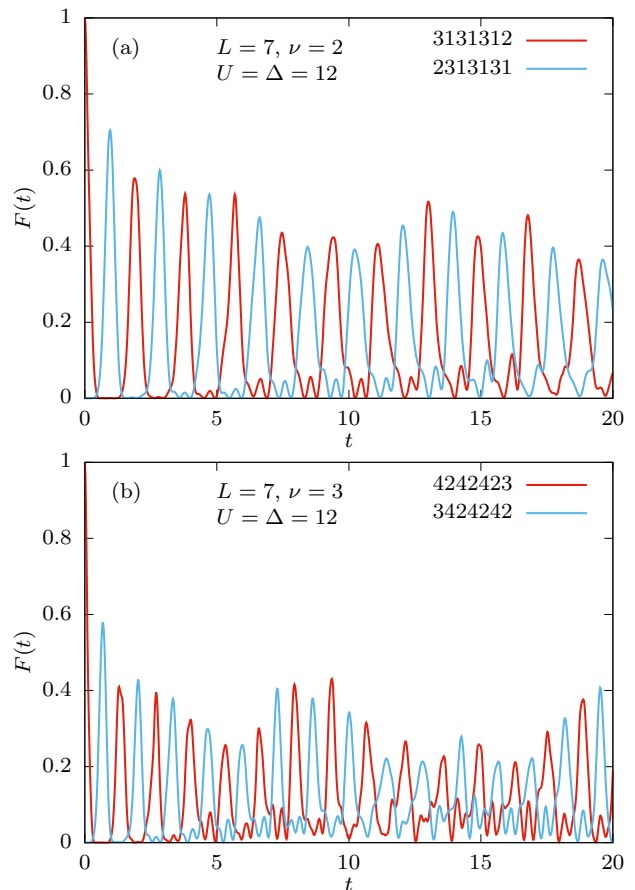A different mapping between the tilted 1D Bose-Hubbard and the PXP model is possible once the stag-

FIG. S4. Evolution of quantum fidelity $F(t) = |\langle \psi_0 | e^{-iHt} | \psi_0 \rangle|^2$ starting from the Néel state $|\psi_0\rangle$ (red) and the amplitude of state transfer, $\mathcal{O}(t) = |\langle \psi | e^{-iHt} | \psi_0 \rangle|^2$, for the anti-Néel state $|\psi\rangle$ (blue). The evolution is governed by the full tilted Bose-Hubbard Hamiltonian with $J = 1$ and $U = \Delta = 12$. (a) Filling factor $\nu = 2$. (b) $\nu = 3$. The Hilbert space size is reduced by removing the configurations with more than 3 particles per site in (a) and more than 4 particles per site in (b).

gered potential term is added to the the model:

$$\hat{H} = -J \sum_{i=1}^{L-1} \left(\hat{b}_i^\dagger \hat{b}_{i+1} + \hat{b}_{i+1}^\dagger \hat{b}_i \right) + \frac{U}{2} \sum_{i=1}^{L} \hat{n}_i \left(\hat{n}_i - 1 \right)$$
$$+ \Delta \sum_{i=1}^{L} i \hat{n}_i + \frac{\delta}{2} \sum_{i=1}^{L} (-1)^{i-1} \hat{n}_i. \tag{S8}$$

The parameter δ determines the energy offset between even and odd lattice sites. The odd ones are now "plus" sites where the δ term is positive, while the even one are "minus" sites where it is negative. This means that for an odd chain of length L there are $N = \frac{L-1}{2}$ minus sites and $N + 1 = \frac{L+1}{2}$ plus sites.

The model in Eq. (S8) has been experimentally studied (see [2] and references therein). Its mapping to the U(1) quantum link model has been already established in the literature, as is the mapping between the U(1) quantum

link model and the PXP model [3]. However, the equivalence of the tilted Bose-Hubbard model with staggered detuning and the PXP model was to our knowledge never explicitly stated, so we will briefly explain it here. This mapping is valid in the regime $U \approx 2\delta \gg J$ and at filling factor $\nu = 1/2$.

When $U \approx 2\delta \gg J$, the second-order process $101 \leftrightarrow 020$ becomes resonant. Nonzero tilt Δ makes other relevant second-order processes such as $100 \leftrightarrow 001$ off-resonant. In this regime and for odd system size L with filling factor $\nu = \frac{L+1}{2L}$, the effective Hamiltonian at second order of the model in Eq. (S8) is fragmented. One of these fragments can be mapped to the PXP model up to some diagonal boundary terms. To find the corresponding state in PXP, one only needs to look at the "minus" sites. Doublons on these sites are mapped to PXP excitations, as the resonant processes cannot create two doublons on two adjacent minus sites. Due to the nature of the resonant process they can never be singly-occupied, and empty minus sites are mapped to non-excited atoms. This means that the corresponding PXP model has length $N = \frac{L-1}{2}$, which is just the number of minus sites.

The Néel states $\bullet\circ\bullet\circ\ldots\bullet\circ$ and $\circ\bullet\circ\bullet\ldots\circ\bullet$ are then mapped to $02000200\ldots02001$ and $100200020\ldots0020$ respectively, while $101010\ldots101$ corresponds to the fully polarized state $\circ\circ\circ\ldots\circ\circ\circ$.
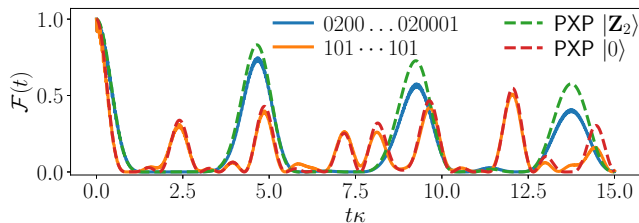

FIG. S5. Time evolution of the fidelity for tilted Bose-Hubbard model with staggered detuning with $L = 13$, $U = 2\delta = 120$, $J = 1$ and $\Delta = 43.3$, and for the PXP model with $N = 6$. The constant κ is the effective hopping strength in each model (see text).

Fig. S5 shows the wave function fidelity over time for the model in Eq. (S8) with $U=2\delta > \Delta \gg J$, and for the PXP model it can be mapped to. To directly compare the two models, we have rescaled the time axis by the constant κ, which takes the value $\sqrt{2}J^{(2)} = \sqrt{2} \times 4J^2U/(U^2-4\Delta^2)$ in the Bose-Hubbard model and Ω in the PXP model. The staggered Bose-Hubbard model oscillates between two product states, $02000200\ldots02001$ and $100200020\ldots0020$, which are the analogs of the Néel states in the PXP model. Overall, the dynamics is seen to be very similar in the two models, with the slight difference between the two being likely due to the boundary terms defined in Eq. (S9) below.

To derive the mapping to the PXP model rigorously, we can separate the Hamiltonian in Eq. (S8) as $\hat{H} = \hat{H}_0 - J\hat{V}$ and perform the Schrieffer-Wolff transformation

[1]. Here $\hat{H}_0$ encompasses all the diagonal terms while V simply corresponds to hopping, which assumes that $\delta, \Delta, U \gg J$. Furthermore, we will only focus on the regime $U = 2\delta$, in which case there are no first order terms. If U is close but not equal to 2δ, then the effective Hamiltonian at first order will contain diagonal terms proportional to $|U - 2\delta|$. Finally, we only focus on the connected component of the second order Hamiltonian that can be mapped to the PXP model, meaning that resonant processes like $02010 \leftrightarrow 11001$ are ignored as these configuration cannot appear in the Hilbert space component of interest.

In the relevant part of the Hilbert space, the only off-diagonal resonant process at second order is $101 \leftrightarrow 020$, which appears with a weight of $\sqrt{2}J^{(2)}$, where $J^{(2)} = \frac{4J^2U}{U^2-4\Delta^2}$. There are also two allowed second-order diagonal processes in the bulk of the chain: $010 \leftrightarrow 010$ and $020 \leftrightarrow 020$. They have a respective weight of $J^{(2)}$ and $2J^{(2)}$. However, as creating a new doublon means emptying two singly-occupied sites, the diagonal matrix elements do not change under the off-diagonal process. The only exception to this is hopping at the boundaries of the chain. For the leftmost site, only hopping to the right and then back is possible, leading to a contribution of $\frac{2J^2}{U-2\Delta}$ instead of $J^{(2)}$. For the rightmost site only hopping to the left is possible and the contribution is $\frac{2J^2}{U+2\Delta}$. This means that not all diagonal matrix elements are the same but they vary between $J^{(2)}N = \frac{L-1}{2}J^{(2)}$ and $(N+1)J^{(2)} = \frac{L+1}{2}J^{(2)}$. However the differences between the diagonal elements are $\mathcal{O}(1)$ and do not scale with L, so they become negligible for large system sizes. All together, the second order Hamiltonian can be mapped to the following model.

$$
\begin{aligned}
\hat{H}_{\text{eff},2} = J^{(2)}N &+ \sqrt{2}J^{(2)}\Big[\hat{X}_1\hat{P}_2 + \hat{P}_{N-1}\hat{X}_N \\
&+ \sum_{j=2}^{N-1} \hat{P}_{j-1}\hat{X}_j\hat{P}_{j+1}\Big] + \frac{2J^2}{U+2\Delta}\hat{n}_1 + \frac{2J^2}{U-2\Delta}\hat{n}_N,
\end{aligned}
\tag{S9}
$$

with $J^{(2)} = 4J^2U/(U^2 - 4\Delta^2)$, $N = (L - 1)/2$, $\hat{n}_j = (1 + \hat{Z}_j)/2$, where $\hat{Z}$ denotes the usual Pauli z matrix. As defined in the main text, $\hat{P}_j = |\circ_j\rangle\langle\circ_j|$ and $\hat{X}_j = |\circ_j\rangle\langle\bullet_j| + |\bullet_j\rangle\langle\circ_j|$. It is worth mentioning that for $U = 2\delta$, the third order effective Hamiltonian is identically zero due to the absence of diagonal elements in the perturbation V (which is simply the hopping) and the next correction only happens at fourth order.

IV. EFFECT OF PERIODIC DRIVING ON $\mathbb{Z}_2$ SCARS

In this section we numerically explore the effect of driving on the stabilization of many-body scars and revival dynamics in the tilted Bose-Hubbard models. Periodic driving was previously shown to enhance and stabilize the revivals in the PXP model [4–6]. The optimal driving

frequency was found to be close to twice that of revivals in the pure PXP model without driving. Given that the tilted Bose-Hubbard model in the resonant regime is equivalent to the PXP model, we anticipate similar effects of periodic driving in this case. We will first review some properties of the driven PXP model.

The following spatially-uniform cosine driving scheme was experimentally implemented in Ref. [4]:

$$\hat{H}(t) = \sum_i \left(\Omega \hat{P}_{i-1} \hat{X}_i \hat{P}_{i+1} + \mu(t) \hat{n}_i \right), \quad \text{(S10)}$$

$$\mu(t) = \mu_0 + \mu_m \cos(\omega t). \quad \text{(S11)}$$

Here, μ_0 is the static detuning, μ_m modulation amplitude and ω driving frequency. The same driving scheme was numerically studied in detail in Ref. [6]. Periodic boundary conditions (PBC) were imposed for simplicity. By scanning the parameter space for the highest time-averaged fidelity, it was determined that the optimal driving parameters for the Néel state $|\mathbb{Z}_2\rangle = |\bullet \circ \bullet \circ \bullet \circ \ldots\rangle$ are $\mu_0/\Omega = 1.15$, $\mu_m/\Omega = 2.67$ and $\omega/\Omega = 2.72$. Driving with these values leads to high revivals whose amplitude remains close to 1 over very long times. Additionally, the driving also strongly suppresses the growth of entanglement entropy.

Ref. [6] has also studied the Floquet modes of the driven PXP model. The Floquet modes are a generalization of eigenstates for periodic time-dependent Hamiltonians $\hat{H}(t + \frac{2\pi}{\omega}) = \hat{H}(t)$. Unlike the eigenstates, the Floquet modes evolve in time, but they are time-periodic with the same periodicity as the driven Hamltonian, $\Phi_n(t + \frac{2\pi}{\omega}) = \Phi_n(t)$. All the Floquet modes $\Phi_n(t = 0)$ of the driven system can be computed by numerically constructing the evolution operator $\hat{U}(T)$ over one driving period $T = \frac{2\pi}{\omega}$ and diagonalizing it.

In the optimal driving regime, the plot of entanglement entropies of all the Floquet modes as a function of their quasienergies consists of two symmetric "arcs" [6]. The two lowest entropy modes also have the highest overlap with the Néel state $|\mathbb{Z}_2\rangle$. One of them is approximately $\Phi_1(0) = (|\mathbb{Z}_2\rangle + |\mathbb{Z}_2'\rangle)/\sqrt{2}$ and the other is close to $\Phi_2(0) = (|\mathbb{Z}_2\rangle - |\mathbb{Z}_2'\rangle)/\sqrt{2}$, while the quasienergy separation between them is $\Delta\epsilon = \epsilon_1 - \epsilon_2 \approx \omega/2$. This provides a simple explanation for the revival dynamics starting from the Néel state, as will be outlined below.

Let us assume that the two idealized states $\Phi_1(0)$ and $\Phi_2(0)$ are indeed exact Floquet modes. The initial state $|\mathbb{Z}_2\rangle$ will then be a superposition of only these two modes

$$\psi(0) = \frac{1}{\sqrt{2}} \Phi_1(0) + \frac{1}{\sqrt{2}} \Phi_2(0) \quad \text{(S12)}$$

and will evolve as

$$\psi(t) = \frac{1}{\sqrt{2}} e^{-i\epsilon_1 t} \Phi_1(t) + \frac{1}{\sqrt{2}} e^{-i\epsilon_2 t} \Phi_2(t) =$$

$$\frac{1}{\sqrt{2}} e^{-i\epsilon_1 t} \left(\Phi_1(t) + e^{i\Delta\epsilon t} \Phi_2(t) \right). \quad \text{(S13)}$$

After one driving period, the two Floquet modes will return to their initial states, but the relative phase will be $e^{i\frac{\omega}{2}\frac{2\pi}{\omega}} = e^{i\pi} = -1$. The wavefunction after one period will therefore be in the anti-Néel state (with an unimportant phase prefactor), $\psi(T) = e^{-i\epsilon_1 T}|\mathbb{Z}_2'\rangle$. It will take two driving periods for the relative phase to again become $+1$ and the wavefunction to return to the initial $|\mathbb{Z}_2\rangle$ state. This is the origin of the period doubling (subharmonic response to periodic driving) which was observed in previous works [4, 6]. We note that the period doubling disappears if the translation symmetry is resolved and the calculations are restricted to the $k = 0$ momentum subspace. In that case, the initial state $(|\mathbb{Z}_2\rangle + |\mathbb{Z}_2'\rangle)/\sqrt{2}$ has high overlap with only a single Floquet mode and trivially oscillates with the same frequency as the periodic drive.
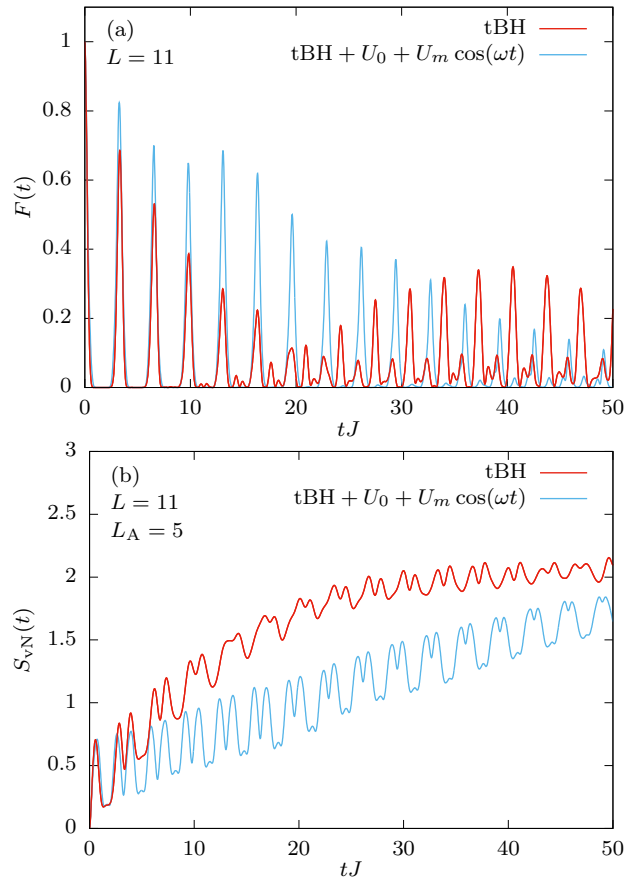

FIG. S6. Comparison of the dynamics in the tilted Bose-Hubbard model without (red) and with periodic driving (blue). System size $L = 11$, maximally 3 particles per site, $J = 1$, $\Delta = 16$, driving parameters $U_0 = 1.85$, $U_m = 3.71$, $\omega = 3.85$. (a) Fidelity. (b) Entanglement entropy for subsystem size $L_A = 5$ sites.

As the tilted Bose-Hubbard model can be mapped to the PXP model in the $U \approx \Delta \gg J$ limit, we also expect to be able to enhance many-body scarring via periodic modulation of the term corresponding to the number of excitations. In the Bose-Hubbard case, such a term is

conveniently provided by the on-site interaction strength U. However, we cannot use periodic boundary conditions due to the linear tilt which would be discontinuous at the boundary. We therefore consider the Bose-Hubbard model with open boundary conditions and periodically modulate the interaction strength $U(t)$,

$$\hat{H}(t) = -J \sum_{i=1}^{L-1} \left(\hat{b}_i^\dagger \hat{b}_{i+1} + \hat{b}_{i+1}^\dagger \hat{b}_i \right)$$
$$+ \frac{U(t)}{2} \sum_{i=1}^{L} \hat{n}_i (\hat{n}_i - 1) + \Delta \sum_{i=1}^{L} i \hat{n}_i, \quad \text{(S14)}$$

with the driving given by

$$U(t) = \Delta + U_0 + U_m \cos(\omega t). \quad \text{(S15)}$$

The driving parameters U_0, U_m and ω, are the static detuning and the modulation amplitude of the interaction strength and the driving frequency, respectively.

The modulation of interaction strength indeed leads to enhanced revivals in the Bose-Hubbard model, see Fig. S6. In particular, the slope of entanglement growth is significantly reduced, with scarred oscillations becoming more pronounced. However, in local observables, such as the density of doublons, the effects of driving are less striking than in the pure PXP model. The reason for more modest enhancement of revivals in the Bose-Hubbard model is the competition between stabilization of revivals within the PXP subspace and the processes which destroy the mapping to PXP model, such as the terms creating 3 or more bosons on a site. Additionally, the optimal driving parameters are not the same as those for the PXP model (up to the trivial rescaling by $\Omega = \sqrt{2}J$ to match the normalization of off-diagonal matrix elements). Increasing the tilt parameter Δ brings the tilted Bose-Hubbard model closer to the PXP model, but it is still necessary to perform a separate optimization of driving parameters.

V. QUANTUM MANY-BODY SCARS IN THE POLARIZED STATE

In the main text we reported the observation of many-body scarring associated with the state that contains no doublons, $|111\ldots\rangle$, or equivalently the fully-polarized state $|\circ\circ\circ\ldots\rangle$ in the PXP model. In this section we provide extensive theoretical evidence for many-body scarring in the polarized state. While the polarized state does not exhibit many-body scarring in the pure PXP model, consistent with previous work [7], it does display weak signatures of non-ergodicity in local observables for sufficiently small systems. In this section, we show that static detuning and its periodic modulation can be used to stabilize the scarring from this initial state. As we will demonstrate below, the many-body scarring in the polarized state is distinct from the previously studied "dynam-

ical freezing" regime associated with $|\circ\circ\circ\ldots\rangle$ state in the PXP model driven by a square pulse protocol [8].
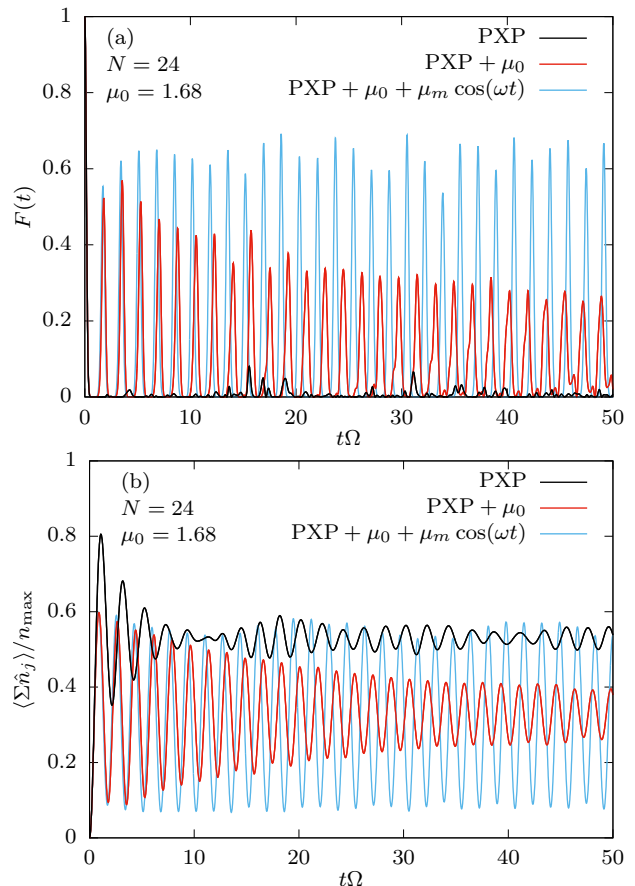

FIG. S7. Comparison of dynamics from the polarized state in the pure PXP model (black), with static detuning only (red), and with both static detuning and periodic driving (blue). System size $N = 24$, driving parameters $\mu_0/\Omega = 1.68$, $\mu_m/\Omega = -0.50$, $\omega/\Omega = 3.71$. (a) Fidelity. (b) Expected total number of excitations normalized by the maximal number of excitations $n_{\max} = N/2$.

A. Pure PXP model

The polarized state $|\circ\circ\circ\ldots\rangle$ is expected to thermalize in the pure PXP model. Nevertheless, the state exhibits some signatures of non-ergodic dynamics in smaller system sizes, such as oscillations in the expectation values of certain local observables. For example, as shown by the black lines in Figs. S7(a) and (b), even though there are no significant revivals in wave function fidelity, some oscillations in the number of excitations are still visible.

A closer look at the eigenstates of the PXP Hamiltonian and their overlap with the polarized state reveals the underlying reason for this behaviour, see Fig. S8. In Fig. S8(a) we plot the overlap of all PXP eigenstates with the Néel state, showing the well known band [9] of scarred eigenstates marked by the red crosses and corresponding
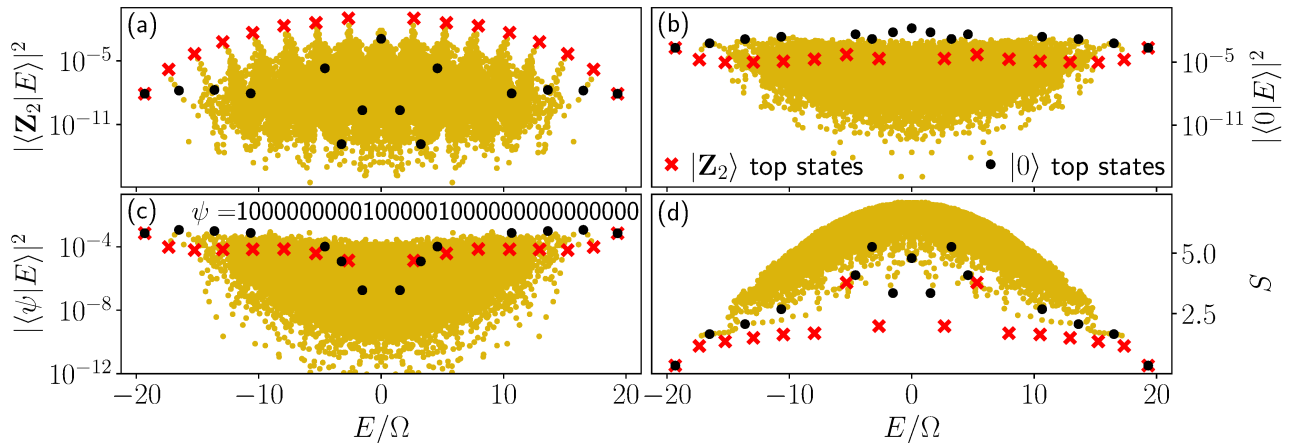
FIG. S8. PXP eigenstates, system size $N = 32$, symmetry sector $\{k = 0,\ p = 1\}$. Overlap with (a) Néel state. (b) polarized state. (c) randomly chosen state. (d) Bipartite entanglement entropies of all eigenstates. The highest-overlap eigenstates in their energy window are marked by red crosses for the Néel state and by black dots for the polarized state.

tower structures. In contrast, there is no such band of high-overlap eigenstates for a randomly chosen state, see Fig. S8(c).The polarized state is between these two cases, as can be observed in Fig. S8(b). Although there is no well defined band of scarred eigenstates as for the Néel state, there is still a number of unusually high-overlap eigenstates which are marked by the black dots. Finally, in Fig. S8(d) we show the entanglement entropies of all eigenstates. The lowest-entropy eigenstates are the Néel state scars (red crosses), but the eigenstates with the highest overlap with the polarized state (black dots) also have lower then average entanglement entropies. Thus, we conclude that the polarized state is poised to develop many-body scarring by a suitable perturbation of the PXP model. We next show that this can be achieved by applying static detuning.

B.   Static detuning and periodic driving in the PXP model

The addition of a static detuning term

$$\hat{H}(\mu_0) = \hat{H}_{\mathrm{PXP}} + \mu_0 \sum_j \hat{n}_j \qquad (\mathrm{S16})$$

results in the appearance of a band of atypical eigenstates with high overlap with the polarized state, as can be observed in Fig. S9. The band is still not well separated from the bulk at lower values of μ_0/Ω, see Figs. S9(a) and (b). At larger values of μ_0/Ω, the energy spectrum starts to split into disconnected bands, as shown in Fig. S9(d). We are interested in the intermediate regime shown in Fig. S9(c), $\mu_0/\Omega \approx 1.68$, where there is a clearly visible band of scarred states, but the bulk of the energy spectrum is still continuous.

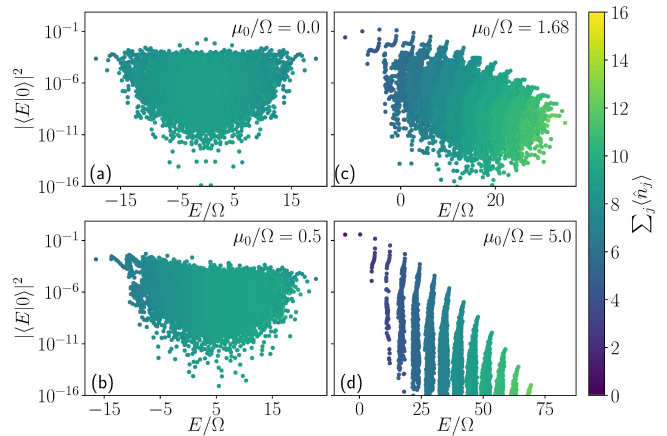In addition to having the highest overlap with the polarized state, the special states are also approximately

FIG. S9. Overlap between the polarized state and the PXP eigenstates in the symmetry sector $\{k = 0,\ p = 1\}$ for $N = 32$. Each subfigure corresponds to a different value of the static detuning, and the color indicates the expectation value of the number of excitations for each eigenstate.

equidistant in energy and have lower entanglement entropy than most other eigenstates. These are all paradigmatic properties of quantum many-body scars. However, one striking difference compared to the Néel state scars is that the highest-overlap states are not concentrated in the middle of the spectrum. Instead, most of them are located at one edge of the energy spectrum, but the band of atypical states still continues well into the higher energy densities, see Fig. S9(c). The fact that special eigenstates are biased towards one end of the spectrum is expected since the detuning potential breaks the particle-hole symmetry of the PXP Hamiltonian [10].

This emergence of scarred eigenstates significantly affects the revival dynamics, as illustrated in Figs. S7 and S10. For the Néel state in Fig. S10(a), the detuning monotonically destroys the revival, until we reach the
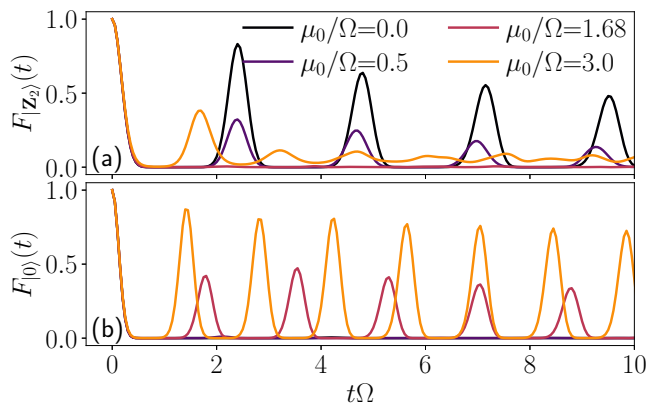
FIG. S10. Revival fidelity for the Néel and polarized states in the symmetry sector $\{k = 0, p = 1\}$ for $N = 32$. (a) Néel state. (b) polarized state. At low detuning only the Néel states revives, while for $\mu_0/\Omega \gg 1$ both states do. However, in the intermediate regime $\mu_0/\Omega \approx 1$ only the polarized state has revivals, while the Néel state thermalizes like the other product states.
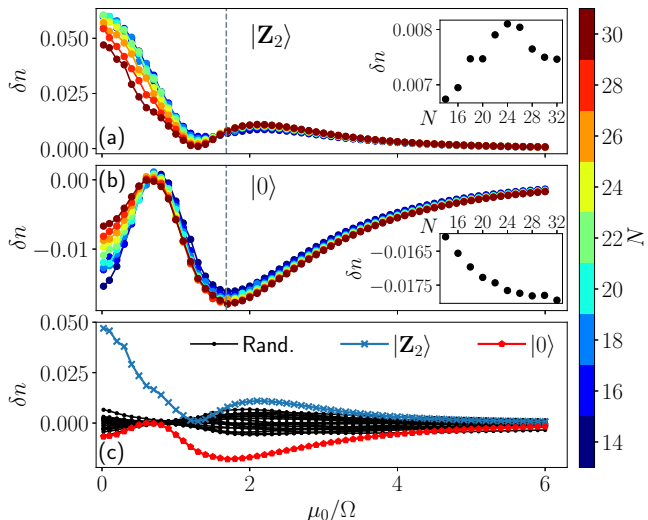

FIG. S11. Difference of expectation value between the diagonal and canonical ensemble for the operator $\frac{1}{N} \sum_j \hat{n}_j$ in the PXP model. (a) Néel state. (b) polarized state. (c) comparison of different states for $N = 30$. The color scale in (a) and (b) corresponds to the system size N, while the insets show the results for various N with μ_0/Ω fixed to 1.68 (along the grey dahsed line).

regime of very large detuning $\mu_0 \gtrsim 3$ which places the Néel state in its own fragment of the Hilbert space. By contrast, for the polarized state in Fig. S10(b) we see the revivals start to emerge at moderate detuning $\mu_0/\Omega \approx 1$. The frequency of the revival is found to match the energy separation between the scarred states in Fig. S9(c). The oscillations in the number of excitations are also enhanced and their frequency has changed to the frequency of fidelity revivals. This is the regime that corresponds

to the many-body scarring observed in experiment. We note that the revivals from the polarized state also persist in the trivial large-detuning limit ($\mu_0 \gtrsim 3$) where the polarized state is effectively in its own fragment of the Hilbert space, similar to the Néel state.

The addition of detuning not only affects the short-time dynamics, but also *infinite-time* expectation values. After a quench, the value of any observable will reach the value predicted by the diagonal ensemble $O_d = \sum_{i,j} O_{i,j} \delta_{i,j} c_j c_i^\star$, where $O_{i,j} = \langle E_i | O | E_j \rangle$ and $c_i = \langle E_i | 0 \rangle$. However we also expect the observable to thermalize towards the value predicted by the canonical ensemble $O_{th} = \text{Tr} \left[\hat{\rho}_{th} \hat{O} \right]$, where $\hat{\rho}_{th} = \frac{1}{\mathcal{Z}} e^{-\beta \hat{H}}$ with $\mathcal{Z} = \text{Tr} \left[e^{-\beta \hat{H}} \right]$ and β the inverse temperature. Note that we also restrict $\hat{H}$ to the symmetry sector invariant under translation and spatial inversion as it is the only one compatible with the $|0\rangle$ state. A large difference between the predictions of these two ensembles for a given initial state is an indicator of the violation of the Eigenstate Thermalization Hypothesis [11, 12]. For the PXP model we will use the operator $\hat{n} = \frac{1}{N} \sum_j \hat{n}_j$, which counts the average number of excitations in the system [13], and denote the difference between the ensemble predictions by δn. The Néel state is most athermal at zero detuning, while the peak for the polarized state occurs around $\mu_0/\Omega = 1.7$, see Fig. S11. For larger values of the detuning these two states become respectively the topmost and ground states, meaning that the temperature is $\pm\infty$ and both ensembles agree exactly.

Finally, in order to stabilize revival and many-body scarring in the polarized state at *late* times, we need to modulate the detuning amplitude, in addition to the static detuning. Using the same driving protocol as for the Néel state in Eq. (S11), we can enhance and stabilize the revivals from the polarized state at late times, see Fig. S7 (blue lines). The optimal driving frequency ($\omega/\Omega = 3.71$) was found to be close to the frequency of revivals in the undriven case with static detuning, while the other two driving parameters ($\mu_0/\Omega = 1.68$, $\mu_m/\Omega = -0.50$) had to be separately optimized for the polarized state and are different from the values obtained for the Néel state. This driving regime and the corresponding Floquet modes $\Phi_n(t = 0)$ were studied in Ref. [6]. There is a single mode that has very high overlap with the polarized state, which explains the revival dynamics in Figs. S7 and S10(b). Note that there is no period doubling in this case.

C. Polarized state in the tilted Bose-Hubbard model

Finally, we confirm that our conclusions about many-body scarring associated with the polarized state also hold in the full tilted Bose-Hubbard model in the regime $U \approx \Delta$, where we expect the effective description to be
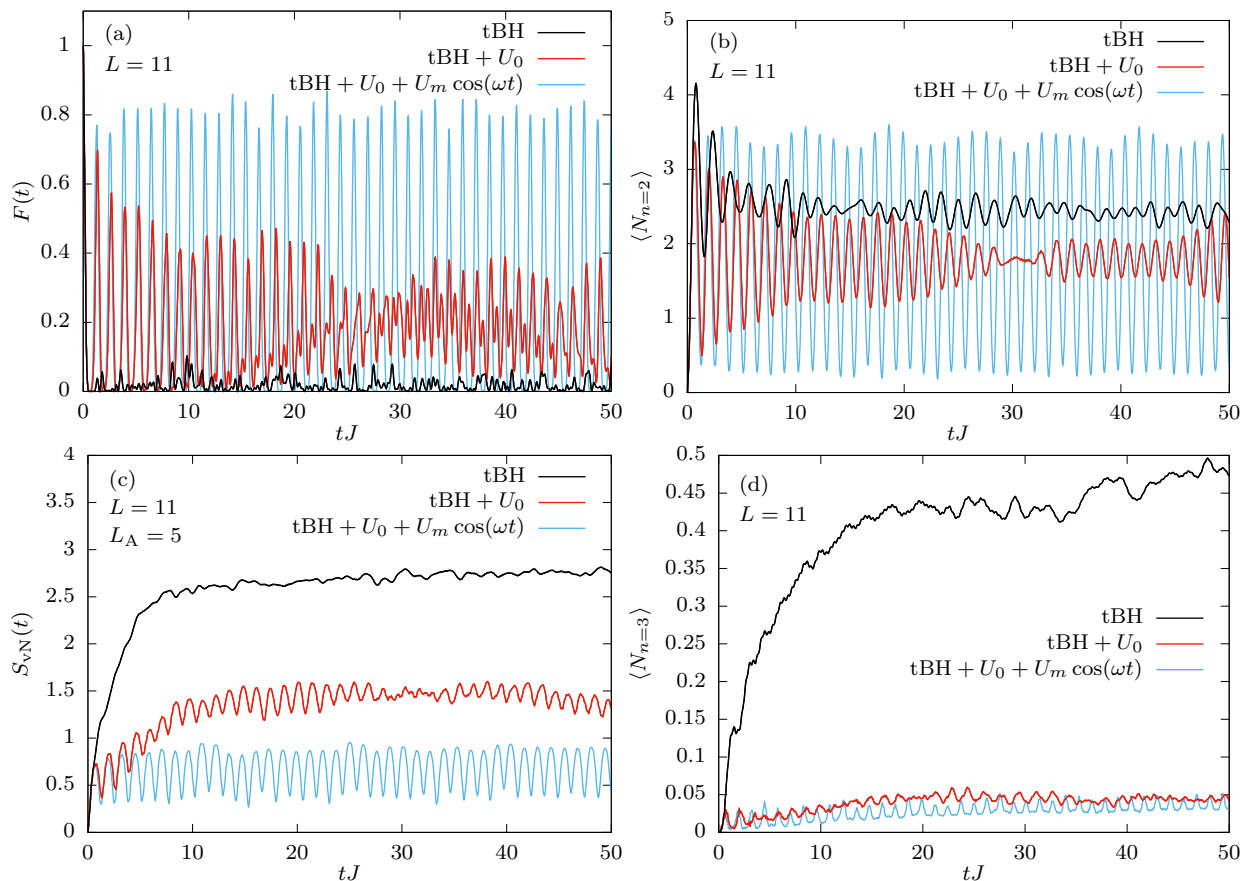
FIG. S12. Comparison of dynamics in the tilted Bose-Hubbard model (black), with static detuning only (red), and with both static detuning and periodic driving (blue). System size $L = 11$, maximally 3 particles per site, $J = 1$, $\Delta = 16$, driving parameters $U_0 = -2.38$, $U_m = 1.54$, $\omega = 4.90$. (a) Fidelity. (b) Expected total number of doublons $N_{n=2}$. (c) Entanglement entropy for subsystem size $L_A = 5$. (d) Expected total number of sites with three particles $N_{n=3}$ (indicates the leakage from the PXP subspace).

close to the PXP model. We will show that the driving leads to a strong suppression of entanglement growth and makes off-resonant the processes that cause leakage out of the PXP subspace.

In Fig. S12 we compare the dynamics at the resonance $U = \Delta$ (black lines, corresponding to the pure PXP model), at $U = \Delta + U_0$ (red lines, corresponding to the PXP model with static detuning), and for $U(t) = \Delta + U_0 + U_m \cos(\omega t)$ (blue lines, corresponding to the periodically driven PXP model). Due to the very fast growth of the Hilbert space size, we restrict the maximal number of bosons per site to 3. The results are consistent with those for the PXP model shown in Fig. S7. Note that the frequency of fidelity revivals in Fig. S12(a) is the frequency of PXP revivals multiplied by a factor of $\sqrt{2}$ which comes from the off-diagonal matrix elements in the Bose-Hubbard model. The expected number of doublons, which is related to the number of PXP excitations is shown in Fig. S12(b).

The growth of entanglement entropy is suppressed by the addition of static detuning and even more by periodic driving, see Fig. S12(c). There are two factors that

contribute to this behaviour. One is the dynamics inside the PXP subspace, where thermalization is suppressed by scarring. The other is related to the leakage out of this subspace, which is represented by the number of sites with 3 particles in Fig. S12(d). The static detuning by itself significantly decreases this quantity, while the periodic driving does not seem to result in a substantial further improvement for the polarized state.

VI. EFFECT OF DETUNING ON THE SPECTRAL STATISTICS OF THE PXP MODEL

In this section we show that the addition of finite detuning to the PXP model does not make this model integrable. We study the energy level spacings $s_n = E_{n+1} - E_n$, which we normalize to have $\langle s_n \rangle = 1$. For an integrable model, $\{s_n\}$ should follow the Poisson distribution, while for a chaotic model we expect to see the Wigner-Dyson distribution. A convenient way to probe level statistics is by computing the so-called $\langle r \rangle$ parame-

ter [14], defined as the average of level spacing ratios:

$$r_n = \frac{\min(s_n, s_{n-1})}{\max(s_n, s_{n-1})}. \tag{S17}$$

For the Poisson statistics, we expect $\langle r \rangle \approx 0.39$, while $\langle r \rangle \approx 0.53$ for Wigner-Dyson. In Fig. S13 we show that
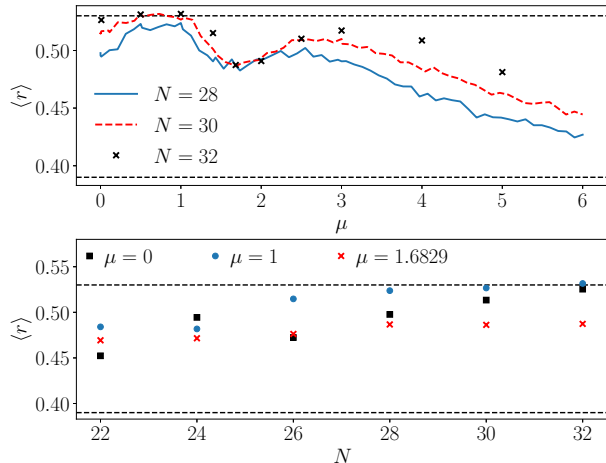

FIG. S13. $\langle r \rangle$ for the PXP model with various system sizes N and detuning μ. For all values of μ shown, the spectral statistics flows towards Wigner-Dyson value, as the $\langle r \rangle$ parameter increases with system size. However the convergence is slower near $\mu = 0$, $\mu = 1.68$, and in general as μ becomes larger.

$\langle r \rangle$ tends towards 0.53 as N increases, for all values of μ. In general, as μ becomes larger, the convergence is slower because the detuning approximately conserves the number of excitations. Beyond that, one can also notice two dips in $\langle r \rangle$ at $\mu = 0$ and $\mu \approx 1.6$, hinting that near these values PXP is close to another integrable model. For pure PXP this had been noted and previously investigated with various other perturbations [15].

The full distribution of the s_n is shown in Fig. S14 for $\mu = 0$, 1, and 1.6829 for $N{=}32$ spins. In all cases, we see that the distribution resembles Wigner-Dyson, even though in the last case it is skewed towards zero.

In conclusion, for any finite value of μ, the PXP model is non-integrable and its level statistics follow the Wigner-Dyson distribution in a large enough system size. Interestingly, the level statistics suggests a proximity to an integrable model at the points where we find good revivals due to scars: at $\mu = 0$ for the Néel state and near $\mu = 1.68$ for the polarized state. These results are in accordance with the discrepancies observed between the diagonal and canonical ensembles in Fig. S11.

VII. SYSTEM-SIZE SCALING OF THE REVIVAL FIDELITY

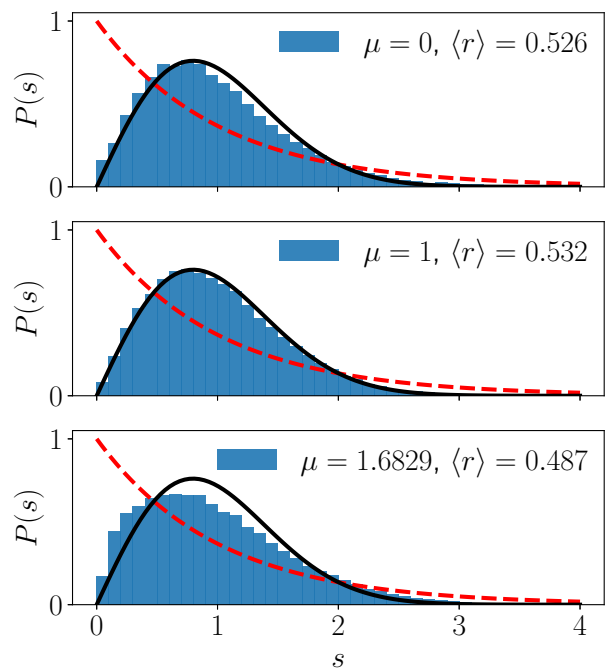An important question concerns the stability of revivals in the thermodynamic limit. In particular, due to

FIG. S14. Distribution of the level spacings after spectrum unfolding for the PXP model with $N{=}32$. The solid black line corresponds to the Wigner-Dyson distribution and the dashed red line to Poisson. In all cases the distribution is close to Wigner-Dyson, even though for $\mu = 1.6829$ it is skewed towards $s = 0$.

the cost of non-linear optimization, the driving parameters were obtained in relatively small systems, therefore it needs to be checked whether the same parameters work as well in large systems. To access dynamics in much larger systems, $L \lesssim 50$ sites, we use TEBD variational method [16] implemented in TenPy package [17]. We employ the second order Trotter decomposition with time step $2.5 \times 10^{-5}/J$ and maximum bond dimension $\chi_{\max} = 3000$. Such a small time step was necessary because some of the quantities we are interested in, e.g., the fidelity density, are sensitive to otherwise negligible fluctuations in the revival peak heights that appear for longer time steps.

Figs. S15 and S16 show the system size scaling of the first three revival peaks for different initial states, both with and without driving. The results were obtained from numerical simulations of the tilted Bose-Hubbard model, Eq. (S14), with open boundary conditions, $\Delta/J = 16$, and maximally 3 particles per site. This particle number limit is an reasonable assumption since the periodically driven interaction strength $U(t) = \Delta + U_0 + U_m \cos(\omega t)$ is large compared to the hopping amplitude J. In the case of global fidelity $F(t)$, we plot the so-called fidelity density $-\ln(F(nT))/L$, where T is the revival period and $n \in \{1, 2, 3\}$. The single-site fidelity $\mathcal{F}_{(1)}(t)$ is a local quantity, so it does not need to be rescaled by the system size L. We therefore simply
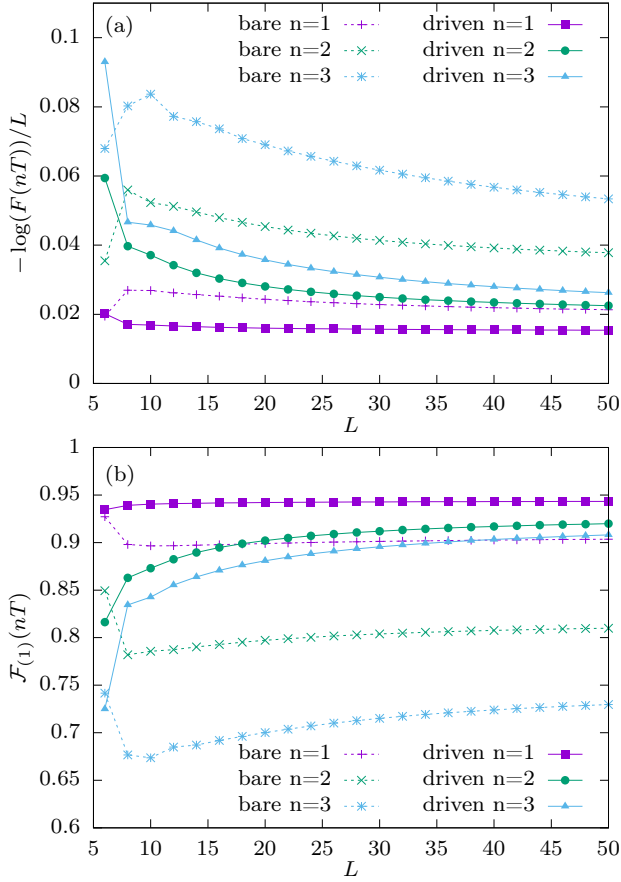
FIG. S15. System size scaling of the first three revival peaks for the Néel state $|\mathbb{Z}_2\rangle = |2020\ldots20\rangle$. Driving parameters $\omega = 3.85$, $U_0 = 1.85$, $U_m = 3.71$. Dashed lines correspond to the bare case and the solid lines to the driven case. (a) Fidelity density. (b) Single-site fidelity.

plot the peak heights $\mathcal{F}_{(1)}(nT)$.

For the Néel state $2020\ldots20$, the fidelity density is expected to converge to a constant value in the limit of large L. This is consistent with our results in Fig. S15(a), where we plot the fidelity density after one, two and three driving periods. The driving parameters are the same for all system sizes, $\omega = 3.85$, $U_0 = 1.85$ and $U_m = 3.71$. Due to the minus sign in the definition, lower fidelity density corresponds to higher revival peaks and vice versa. As can be observed in Fig. S15(a), periodic driving leads to increased revivals over a broad range of system sizes and there is no indication that this will change for $L > 50$. The revivals are decaying with time, but the decay is significantly slower when the driving is turned on. We can thus conclude that periodic driving with these parameters both enhances and stabilises the revivals, even in relatively large systems.

The scaling of the single-site fidelity can be observed in Fig. S15(b). This experimentally measurable quantity represents a tight upper bound for the global fidelity when the system is initialized in a product state, see Section **??**. The results are similar to those for the global

fidelity. In all cases, the revival heights are rapidly converging towards a constant value. Again, the revivals in driven systems are significantly higher than those without driving and the difference between them increases with time.
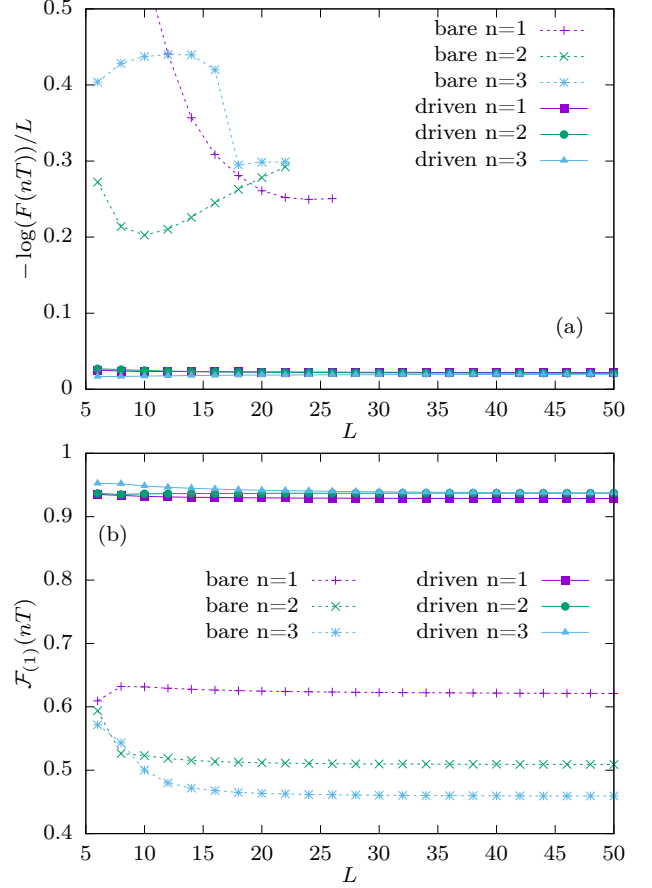

FIG. S16. System size scaling of the first three revival peaks for the polarized state $|111\ldots111\rangle$. Driving parameters $\omega = 4.90$, $U_0 = -2.38$, $U_m = 1.54$. Dashed lines correspond to the bare case and the solid lines to the driven case. Data points are missing in cases where there are no local maxima. (a) Fidelity density. (b) Single-site fidelity.

The effects of periodic driving are even more striking with the polarized state $111\ldots111$ as the initial state, as shown in Fig. S16. There are no notable revivals in global fidelity when the driving is turned off. The dashed lines in Fig. S16(a) correspond to irregular minor local maxima which are present in smaller systems. Even these local maxima disappear with increasing system size, which explains why some data points are missing. In contrast, driving with parameters $\omega = 4.90$, $U_0 = -2.38$ and $U_m = 1.54$ produces very high revivals which do not decay, either with time or with system size. The single-site fidelity tells a similar story, see Fig. S16(b), however in this case there are revivals even in the absence of driving, consistent with dynamics of local observables in Fig. S7(b).

Finally, we note that the Néel and polarized states are

the only two initial product states for which we were able to find optimal driving parameters that lead to robust revivals at late times. This is true both for the tilted Bose-Hubbard model, Eq. (S14) in the $\Delta \approx U$ regime, and for the PXP model with a spatially uniform driving protocol. For other initial states, such as $\mathbb{Z}_4$ state

with an excitation on every fourth site or, equivalently, $20112011\ldots 2011$ in the tilted Bose-Hubbard model, it is possible to stabilize a small number of revivals at short times. In contrast to the Néel and polarized states, these revivals are found to decay quickly with time as well as with system size.

[1] S. Bravyi, D. P. DiVincenzo, and D. Loss, Ann. Phys. **326**, 2793 (2011).
[2] J. C. Halimeh, R. Ott, I. P. McCulloch, B. Yang, and P. Hauke, Phys. Rev. Research **2**, 033361 (2020).
[3] F. M. Surace, P. P. Mazza, G. Giudici, A. Lerose, A. Gambassi, and M. Dalmonte, Phys. Rev. X **10**, 021041 (2020).
[4] D. Bluvstein, A. Omran, H. Levine, A. Keesling, G. Semeghini, S. Ebadi, T. T. Wang, A. A. Michailidis, N. Maskara, W. W. Ho, S. Choi, M. Serbyn, M. Greiner, V. Vuletić, and M. D. Lukin, Science **371**, 1355 (2021).
[5] N. Maskara, A. A. Michailidis, W. W. Ho, D. Bluvstein, S. Choi, M. D. Lukin, and M. Serbyn, Phys. Rev. Lett. **127**, 090602 (2021).
[6] A. Hudomal, J.-Y. Desaules, B. Mukherjee, G.-X. Su, J. C. Halimeh, and Z. Papić, Phys. Rev. B **106**, 104302 (2022).
[7] H. Bernien, S. Schwartz, A. Keesling, H. Levine, A. Omran, H. Pichler, S. Choi, A. S. Zibrov, M. Endres, M. Greiner, V. Vuletić, and M. D. Lukin, Nature **551**, 579 (2017).
[8] B. Mukherjee, A. Sen, D. Sen, and K. Sengupta, Phys. Rev. B **102**, 075123 (2020).
[9] C. J. Turner, A. A. Michailidis, D. A. Abanin, M. Serbyn, and Z. Papić, Nature Physics **14**, 745 (2018).
[10] C. J. Turner, A. A. Michailidis, D. A. Abanin, M. Serbyn, and Z. Papić, Phys. Rev. B **98**, 155134 (2018).
[11] J. M. Deutsch, Phys. Rev. A **43**, 2046 (1991).
[12] M. Srednicki, Phys. Rev. E **50**, 888 (1994).
[13] Z. Yao, L. Pan, S. Liu, and H. Zhai, "Quantum many-body scars and quantum criticality," (2021), arXiv:2108.05113 [cond-mat.quant-gas].
[14] V. Oganesyan and D. A. Huse, Phys. Rev. B **75**, 155111 (2007).
[15] V. Khemani, C. R. Laumann, and A. Chandran, Phys. Rev. B **99**, 161101 (2019).
[16] G. Vidal, Phys. Rev. Lett. **91**, 147902 (2003).
[17] J. Hauschild and F. Pollmann, SciPost Phys. Lect. Notes , 5 (2018), code available from https://github.com/tenpy/tenpy, arXiv:1805.00055.